PHYSICAL REVIEW D **87,** 025010 (2013)

Instabilities of an anisotropically expanding non-Abelian plasma: 3D + 3V discretized hard-loop simulations

Maximilian Attems,[1] Anton Rebhan,[1] and Michael Strickland[2,3]

[1]*Institut für Theoretische Physik, Technische Universität Wien, Wiedner Hauptstrasse 8-10, A-1040 Vienna, Austria*
[2]*Physics Department, Gettysburg College, Gettysburg, Pennsylvania 17325, USA*
[3]*Frankfurt Institute for Advanced Studies, Ruth-Moufang-Strasse 1, D-60438, Frankfurt am Main, Germany*

(Received 11 September 2012; published 3 January 2013)

We study the (3 + 1)-dimensional evolution of non-Abelian plasma instabilities in the presence of a longitudinally expanding background of hard particles using the discretized hard-loop framework. The free streaming background dynamically generates a momentum-space anisotropic distribution which is unstable to the rapid growth of chromomagnetic and chromoelectric fields. These fields produce longitudinal pressure that works to isotropize the system. Extrapolating our results to energies probed in ultrarelativistic heavy-ion collisions we find, however, that a pressure anisotropy persists for a few fm/c. In addition, on time scales relevant to heavy-ion collisions we observe continued growth of plasma instabilities in the strongly non-Abelian regime. Finally, we find that the longitudinal energy spectrum is well described by a Boltzmann distribution with increasing temperature at intermediate time scales.

DOI: 10.1103/PhysRevD.87.025010 PACS numbers: 11.15.Bt, 11.10.Wx, 12.38.Mh, 25.75.−q

I. INTRODUCTION

One of the major outstanding questions in the theoretical understanding of ultrarelativistic heavy-ion collisions concerns the thermalization and isotropization of the quark gluon plasma. Empirical evidence in favor of fast thermalization and isotropization was provided by ideal relativistic hydrodynamical models. The success of these models to describe the collective flow observed at the relativistic heavy ion collider (RHIC) suggested that one generated thermal and isotropic matter at time scales on the order of 0.5 fm/c after the initial nuclear impact [1–4]. Based on this success there was a concerted effort to include corrections due to the finite shear viscosity of the plasma [5–27]. Second order viscous hydrodynamics is now widely used to model collisions at both RHIC and the Large Hadron Collider (LHC).

In recent years, however, studies have shown that there is an insensitivity to the assumed momentum-space anisotropy of the plasma, with the data also being consistent with initially large momentum-space anisotropies [22,28]. In addition, studies based on the conjectured anti de Sitter/conformal field theory (AdS/CFT) correspondence have shown that, although viscous hydrodynamical behavior emerges quickly in the strong coupling limit, there are still sizable momentum-space anisotropies present that persist over the entire lifetime of the plasma [29–31]. Based on this, extensions of viscous hydrodynamics that can accommodate large momentum-space anisotropies have been developed [28,32–39]. Currently the question of the degree of momentum-space isotropy of the quark gluon plasma generated in heavy-ion collisions is an open question. In this paper we study the role played by collective unstable modes of the chromomagnetic and chromoelectric fields in restoring momentum-space isotropy of an expanding quark gluon plasma (QGP).

It has been shown using both kinetic theory and diagrammatic methods that when the local particle distribution function of a weakly coupled QGP is anisotropic in momentum space, the system is unstable to the rapid growth of soft gauge fields [40–50]. This instability has been dubbed the chromo-Weibel instability in reference to the Abelian analogue of this instability first discussed by Weibel [51]. In the weak-field regime the chromo-Weibel instability initially causes exponential growth of transverse chromomagnetic and chromoelectric fields; however, due to non-Abelian interaction between the fields, exponentially growing longitudinal chromomagnetic and chromoelectric fields are induced that grow at twice the rate of the transverse field configurations. As a result, one finds strong gauge-field self-interaction at late times due to high-amplitude chromoelectric and chromomagnetic fields and in order to reach quantitative conclusions numerical simulations are necessary.

The initial numerical studies of the time evolution of the chromo-Weibel instability were performed assuming a static momentum-space anistropic (nonexpanding) system and utilized discretizations of the gauge-invariant hard-loop action. The hard-loop action used includes the self-consistent gauge-invariant modification of all n-point functions in the hard-loop limit [52]. The resulting discretized dynamical equations were solved in temporal axial gauge using a regular lattice to describe space and either a discrete lattice [53–55] or an expansion in spherical harmonics [56–60] to describe the velocity space of the hard particles. From the three-dimensional static box simulations one found that exponential field growth ceased when the vector potential amplitude became on the order of $A_{\text{non-Abelian}} \sim p_s/g \sim \sqrt{f_h} p_h$, where p_h is the characteristic momentum of the hard particles, e.g., $p_h \sim Q_s$ for color glass condensate (CGC) initial conditions, f_h is the

 © 2013 American Physical Society

angle-averaged occupancy at the hard scale, and p_s is the characteristic soft momentum of the fields ($p_s \sim g\sqrt{f_h} p_h$). This partial saturation occurs at a scale where the chromofields are not yet strong enough to have O(1) effects on the hard particle distribution, suggesting that isotropization in non-Abelian plasmas is parametrically slower than in the Abelian case. After the exponential growth ceased, a slower linear growth of field energy densities was observed. This linear growth was associated with a cascade of energy pumped into the soft modes to higher momentum modes through nonlinear gauge-field self-interactions [56–58]. The resulting spectrum of soft gauge field excitations was shown to have a power-law spectrum scaling like $f \sim \alpha_s^{-1} p_s^{-2}$ for SU(N_c) with $N_c \in \{2, 3, 4, 5\}$ [55,57,61]. Studies using classical-statistical Yang-Mills simulations also found saturation of gauge-field growth with an associated gauge-field power-law spectrum; however, these studies found saturation only in a regime where backreaction on the hard modes is already strong, with a different scaling consistent with $f \sim \alpha_s^{-1} p_s^{-4/3}$ [62–66].

The presence of instabilities in weakly coupled momentum-space anisotropic systems seems to be generic and independent of the hard-loop approximation, the gauge group, and, in large part, the type of theory considered (including, of course, the weak-coupling limit of supersymmetric gauge theories [67,68]). They have been observed in numerical solutions to the full Boltzmann-Vlasov equations that go beyond the hard-loop approximation [69–71]. As mentioned previously, analogous instabilities have been observed in numerical simulations of pure classical-statistical Yang-Mills dynamics [62–66]. As a result, obtaining a detailed understanding of the chromo-Weibel instability's effect on the isotropization and thermalization of the matter created in ultrarelativistic heavy-ion collisions is of utmost importance. There have been many works that have addressed pieces of the puzzle [47,61,72–75]. Recently there has been a highly impressive effort to parametrically estimate the effect of plasma instabilities on the quark gluon plasma thermalization time [76,77]; however, being a parametric estimate it does not yet fully answer the question or lend itself to extrapolations to realistic couplings.

In order to understand the precise role the chromo-Weibel instability plays in ultrarelativistic heavy-ion collisions it is necessary to include the effect of the strong longitudinal expansion of the matter, particularly during its earliest stages. For the first few fm/c of the quark gluon plasma's lifetime the longitudinal expansion dominates the transverse expansion which only starts to become important at time scales on the order of 4–5 fm/c. Therefore, to good approximation, one can understand the early time dynamics of the quark gluon plasma by only considering longitudinal dynamics. The first study to look at the effect of longitudinal expansion was done in the context of pure Yang-Mills dynamics initialized with CGC initial conditions onto which small-amplitude rapidity fluctuations were added [78,79]. The initial small-amplitude fluctuations result from quantum corrections to the classical dynamics [80,81]. Numerical studies have shown that adding spatial-rapidity fluctuations results in growth of chromomagnetic and chromoelectric fields with amplitudes $\sim \exp(2m_D^0\sqrt{\tau/Q_s})$ where m_D^0 is the initial Debye screening mass and τ is the proper time. This growth with $\exp(\sqrt{\tau})$ was predicted by Arnold *et al.* based on the fact that longitudinal expansion dilutes the density, thereby causing the chromo-Weibel unstable growth rate decrease in time [47].

Since the pioneering study of Refs. [78,79], others are now investigating the evolution of instabilities in classical Yang-Mills [66,82] and scalar ϕ^4 [83] including longitudinal expansion. In addition, a parallel effort to incorporate longitudinal expansion into the hard-loop framework was begun with the first results being semianalytic solutions for Abelian theories that also showed the characteristic $\exp(\sqrt{\tau})$ growth seen in the earlier classical Yang-Mills simulations, as well as rather complex early-time behavior [84]. In the hard-loop framework the longitudinal expansion has thus far been included only in the limit that the hard particles are free streaming. In this case it is possible to introduce a set of auxiliary variables similar to the static hard-loop W fields which account for the time-evolving momentum-space anisotropy of the hard particle distribution.

The Abelian semianalytic solutions of Ref. [84] were shortly followed by numerical solutions of the resulting coupled $SU(2)$ Vlasov-Yang-Mills equations in the simplified case that the vector potential $\mathbf{A}$ and its conjugate momenta $\mathbf{\Pi}$ were homogeneous in the transverse directions [85]. Coupling these transversally homogeneous fields to the fully three-dimensional hard-particle velocity distribution resulted in "1D + 3V" simulations of the resulting dynamics.[1] This study found that, in the case of non-Abelian $SU(2)$ fields, one also observed growth with $\exp(\sqrt{\tau})$ that was only briefly curtailed when the magnitude of the transverse and longitudinal gauge field energies became of the same order. In addition, the 1D + 3V simulations did not see a Kolmogorov cascade at late times.

The problem with such dimensionally reduced studies is that they can be misleading. In fact, one finds in the static box case very different late-time behavior if one allows for either effective one-dimensional dynamics or fully three-dimensional dynamics. One is therefore motivated to determine the full 3D + 3V dynamics in the presence of a longitudinally expanding background. In addition, since the 1D + 3V paper was written it was realized that the initial conditions used were not sufficiently generic and that including initial current fluctuations dramatically

[1]Since, in practice, the ultrarelativistic limit $|\mathbf{v}| \to 1$ is used, the three-dimensional velocity space is further reduced to a two-dimensional space (the surface of a three-sphere).

reduces the previously observed delayed onset of growth of unstable modes [86]. One would therefore like to also use this type of initial condition in the full study.

In this paper, we present the necessary 3D + 3V dynamical equations for so-called hard-expanding-loops (HELs), discretize them in τ-η-$\mathbf{x}_\perp$ coordinates, and solve them numerically. For this purpose we use anisotropic lattices with spatial sizes on the order of $N_\perp^2 \times N_\eta \sim 40^2 \times 128$. At each point on the lattice we also have auxiliary fields $\mathcal{W}$ that are discretized on a velocity lattice with size $N_\phi \times N_u \sim 32 \times 128$ amounting to 4096 auxiliary fields per lattice site. Needless to say this presents a computational challenge that requires parallelization of the resulting code. For the initial conditions we use variants of the initial conditions specified in Ref. [86] in which we have added the possibility of initializing an adjustable spectrum of discrete longitudinal fluctuations. As in our previous studies, the dimensional parameters necessary to fix the initial conditions such as the gluon number density etc. are obtained within the CGC framework.

We find that, apart from a delay of the onset of the unstable mode growth due to transverse dynamics, the overall behavior of the three-dimensional solutions is very similar to the one-dimensional case. We find that the chromo-Weibel instability acts to restore isotropy in the system by inducing large longitudinal field pressure. In contrast to the fixed-anisotropy 3D + 3V studies, we do not see a saturation of the instability on time scales relevant for heavy-ion collisions. In order to address the question of the spectrum of the resulting field configurations we study the longitudinal Fourier modes of the energy density. We find that the longitudinal energy spectrum looks like a Boltzmann distribution while remaining anisotropic in momentum space. Extrapolating to energies appropriate for LHC collisions, we find that the momentum-space anisotropy persists for approximately 6 fm/c. We show that the isotropization time is primarily determined by the assumed magnitude of initial current fluctuations.

The structure of the paper is as follows: In Sec. II we briefly review the expectations one has for unstable mode growth in an expanding background. In Sec. III we review the derivation of the hard-loop equations of motion in a longitudinally free streaming expanding background. In Sec. IV we discuss the method we used to fix the physical scales in our simulation and discuss the initial conditions used. In Sec. V we define the various observables that we will measure during the lattice evolution. In Sec. VI we present our main results and interpret our findings. In Sec. VII we conclude and give an outlook for the future. In three appendixes we collect details concerning the numerical solution of the lattice equations of motion.

II. GENERAL DISCUSSION

Before proceeding to the presentation of the hard-loop equations of motion and their subsequent numerical solution, we will quickly review the presence of instabilities in a momentum-space anisotropic plasma and consider how this changes in an expanding plasma. In a longitudinal free streaming expansion the soft scale is time dependent. Since the density of the free streaming particles drops like $n \sim 1/\tau$ and $m_D^2(\tau) \propto n/p_{\mathrm{hard}}$, we have

$$m_D(\tau) \sim m_D\left(\frac{\tau}{\tau_{\mathrm{iso}}}\right)^{-1/2}, \tag{2.1}$$

where m_D is the "isotropic" Debye mass defined at a time $\tau = \tau_{\mathrm{iso}}$.

At a given proper time we can quantify the degree of plasma anisotropy via ξ

$$\xi = \frac{1}{2}\frac{\langle p_T^2\rangle}{\langle p_z^2\rangle} - 1, \tag{2.2}$$

where p_T and p_z are the transverse and longitudinal (beam line direction) particle momenta in the local reference frame. For a longitudinal free streaming expansion p_T is constant while $p_z \sim 1/\tau$ and as a result one has $\xi_{\mathrm{f.s.}} = (\tau/\tau_{\mathrm{iso}})^2 - 1$.[2]

As we will discuss in Sec. IV, we assume that a plasma description becomes possible after a finite point in proper time τ_0. The ratio $\tau_{\mathrm{iso}}/\tau_0$ then parametrizes the initial momentum-space anisotropy. If this were equal to one, the plasma would start out isotropic and become anisotropic with $\xi > 0$ at subsequent times. However, motivated by the results obtained within the CGC framework [87] we consider the case that the plasma already has a strong oblate ($\xi > 0$) momentum anisotropy at τ_0, which will be modeled by having $\tau_{\mathrm{iso}} \ll \tau_0$ regardless of the fact that a plasma description is certainly not possible at times earlier than τ_0. By the same token, m_D, the isotropic Debye mass at the (fictitious) time τ_{iso}, is just a parameter characterizing our free streaming background of hard plasma particles.

At a given proper time τ, and hence fixed plasma anisotropy, there is a three-dimensional band of soft unstable modes associated with a fluctuation wave vector $\mathbf{k}$. For an oblate distribution the unstable modes with the largest growth rate have $\mathbf{k} \parallel \hat{\mathbf{n}}$ where $\hat{\mathbf{n}}$ is the anisotropy direction [46]. The oblate unstable modes can be classified as either transverse magnetic (α) or mixed ($-$) modes. The mixed modes with finite transverse momentum extend out from the anisotropy direction to a fixed angle of $\theta = \arctan(k_T/k_z) = \pi/4$ beyond which they are stable. The α modes, on the other hand, are unstable for any transverse momentum.

In Fig. 1 we show the range of unstable modes for both types of modes. We show the case of $\xi = 10$ with the

[2]The magnitudes of p_T and p_z stated are the "expected" values for the transverse and longitudinal momentum of a particle in the system. These can be be defined formally as $p_T = \sqrt{\langle p_T^2\rangle n_{\mathrm{iso}}/n}$ and $p_z = \sqrt{\langle p_z^2\rangle n_{\mathrm{iso}}/n}$ where the averages represent integrals using the one-particle distribution and n is the number density.

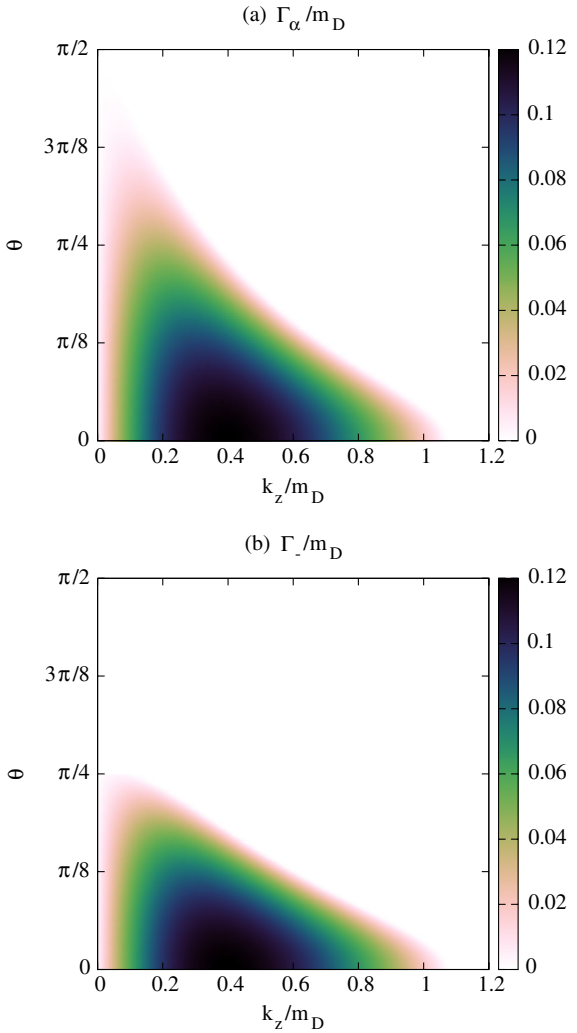

FIG. 1 (color online). Unstable mode growth rates (a) Γ_α/m_D and (b) Γ_-/m_D for $\xi = 10$ as a function of k_z/m_D and $\theta = \arctan(k_T/k_z)$ where m_D is the Debye mass at the proper time $\tau_{\rm iso}$.

understanding that the qualitative features are the same for all $\xi > 0$. In a longitudinally expanding plasma, longitudinal momenta are redshifted in time, but transverse momenta are unaffected. As a result, the mixed unstable modes which have any finite transverse momentum will eventually become stable. The α-mode growth rate decreases rapidly as one increases θ, so while they are technically unstable at all times, the growth rate of any mode which is not purely longitudinal becomes negligible at late times. Thus, at late times the system will be dominated by the dynamics of unstable modes with (nearly) longitudinal wave vectors.[3]

In order to gain a qualitative understanding of the dynamics we can therefore focus our attention on the unstable mode spectrum for purely longitudinal modes.

[3]For a more detailed discussion of the dynamics of stable and unstable modes in an anisotropically expanding plasma see Ref. [86].

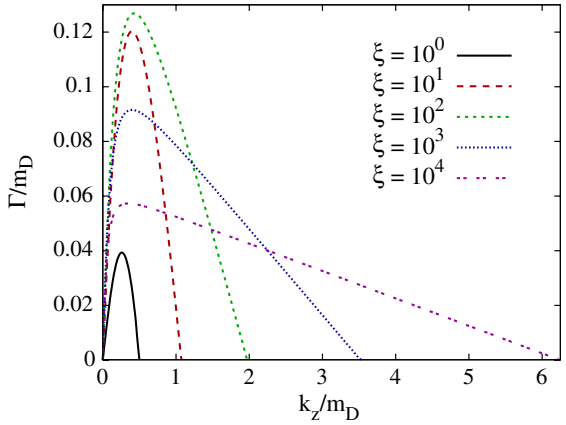

FIG. 2 (color online). Unstable mode growth rate Γ/m_D for fixed ξ as a function of k_z/m_D where m_D is the Debye mass at the proper time $\tau_{\rm iso}$.

In Fig. 2 we plot the unstable mode growth rate for purely longitudinal modes for $\xi \in \{10^0, 10^1, 10^2, 10^3, 10^4\}$. From this figure we can see that there is a band of modes with positive unstable growth rate for longitudinal momenta $k_z \in (0, k_{z,\rm max})$ and there is a well-defined maximum growth rate Γ^* at each value of ξ. As ξ increases $k_{z,\rm max}$ increases and for $\xi \gtrsim 10^2$ one finds that Γ^* decreases monotonically. This means that in an expanding plasma, more and more modes will become unstable as a function of proper time, but at the same time their growth rate is being reduced by the dilution of the plasma due to the longitudinal expansion.

It is possible to derive asymptotic relations for $k_{z,\rm max}$ and Γ^* for large ξ [54]. One finds that

$$\lim_{\xi \gg 1} k_{z,\rm max} \sim m_D(1+\xi)^{1/4}. \tag{2.3}$$

Using this we can determine the approximate proper time dependence of $k_{z,\rm max}$ for a longitudinal free streaming expansion

$$\lim_{\tau \gg \tau_{\rm iso}} k_{z,\rm max} \sim m_D\left(\frac{\tau}{\tau_{\rm iso}}\right)^{1/2}. \tag{2.4}$$

Applying the same methodology to Γ^* one finds

$$\lim_{\tau \gg \tau_{\rm iso}} \Gamma^* \sim m_D(\tau) \sim m_D\left(\frac{\tau}{\tau_{\rm iso}}\right)^{-1/2}. \tag{2.5}$$

As a result, we can estimate the late time unstable growth by integrating Γ^* to obtain

$$N(\tau) \sim \exp\left(m_D \int_{\tau_0}^{\tau} d\tau' \left(\frac{\tau'}{\tau_{\rm iso}}\right)^{-1/2}\right), \sim \exp(2m_D\sqrt{\tau\tau_{\rm iso}}), \tag{2.6}$$

where we have suppressed an overall multiplicative constant. We therefore see that the primary effect of longitudinal expansion will be to change the late time growth from being a pure exponential, as was the case in a static box,

to $\exp(\sqrt{\tau})$. To determine the precise nature of the dynamics on time scales relevant for heavy-ion collisions, however, requires determining the full time evolution of all stable and unstable modes and properly taking into account their interactions. We will now recall the derivation of the necessary dynamical equations to be solved numerically.

III. HARD-EXPANDING-LOOP EQUATIONS OF MOTION

Our study is based upon the hard-loop approximation, which assumes a separation of scales between the momenta of hard particles p_s and the momenta of soft collective fields $p_s \sim g\sqrt{f_h}p_h \ll p_h$ by a sufficiently small gauge coupling g. This separation obviously requires that f_h is parametrically smaller than $1/g^2$. In an anisotropic plasma, f_h is moreover direction dependent and what actually enters in the calculation of the parameters at the soft scale are gradients $\partial f_h/\partial \mathbf{p}_h$. In terms of the anisotropy parameter ξ this means that at parametrically large ξ the hard-loop approximation is applicable only as long as $\xi^{1/2} f_h$ is parametrically smaller than $1/g^2$.

Because we are interested in investigating within the hard-loop framework the earliest stages of the evolution of a quark gluon plasma, which according to the CGC framework is born with overpopulated distribution functions and with large anisotropy, we shall treat the degree of anisotropy formally as being of order 1 compared to g, and f_h of order $g^{-2+\epsilon}$. Eventually, we boldly extrapolate our results to the very limits of the hard-loop framework by setting $\epsilon = 0$ and matching with CGC parameters for the initial density and a strong coupling g that is numerically even larger than 1.[4] This matching to CGC parameters is specified in Sec. IV; in the following we recapitulate the hard-expanding-loop equations, which we have discussed in detail before in Ref. [85], and make the resulting equations explicit for the case at hand, the fully (3 + 1)-dimensional evolution.

A. Longitudinally expanding free streaming background solution

In the hard-loop approximation, the color neutral background distribution function $f_0(\mathbf{p}, \mathbf{x}, t)$ for the hard plasma particles has to satisfy

$$v \cdot \partial f_0(\mathbf{p}, \mathbf{x}, t) = 0, \qquad v^\mu = p^\mu/p^0. \tag{3.1}$$

This is trivially solved by a stationary distribution which only depends on the momenta. Another solution is obtained by considering a plasma with boost-invariant longitudinal expansion, which we take as an approximation for the initial stage of a heavy-ion collision where the transverse extent of the system is taken as sufficiently large. Assuming isotropy in transverse directions, f_0, which is a Lorentz scalar, can be written as [88,89]

$$f_0(\mathbf{p}, x) = f_0(p_\perp, p^z, z, t) = f_0(p_\perp, p'^z, \tau), \tag{3.2}$$

where the Lorentz-boosted longitudinal momentum is

$$\begin{aligned} p'^z &= \gamma(p^z - \beta p^0), & \beta &= z/t, \\ \gamma &= t/\tau, & \tau &= \sqrt{t^2 - z^2}, \end{aligned} \tag{3.3}$$

with $p^0 = \sqrt{p_\perp^2 + (p^z)^2}$ for ultrarelativistic (massless) particles.

Switching to comoving coordinates

$$\begin{aligned} t &= \tau\cosh\eta, & \beta &= \tanh\eta, \\ z &= \tau\sinh\eta, & \gamma &= \cosh\eta, \end{aligned} \tag{3.4}$$

we have curvilinear coordinates $x^\alpha = (x^\tau, x^i, x^\eta) = (\tau, x^1, x^2, \eta)$ where here and elsewhere in the text indices $i, j, \ldots$ correspond to the two transverse spatial directions while greek indices from the beginning of the alphabet refer to the comoving spacetime coordinates. In these new coordinates the metric reads

$$ds^2 = d\tau^2 - d\mathbf{x}_\perp^2 - \tau^2 d\eta^2 = g_{\alpha\beta}(\tau) dx^\alpha dx^\beta, \tag{3.5}$$

but we shall continue to write our equations explicitly in terms of ordinary derivatives and not deal with spacetime covariant derivatives. The gauge-covariant derivative thus always means[5] $D_\alpha = \partial_\alpha - ig[A_\alpha, \cdot]$.

The field strength tensor is defined as $F_{\alpha\beta} = \partial_\alpha A_\beta - \partial_\beta A_\alpha - ig[A_\alpha, A_\beta]$ also in the comoving coordinates (with all indices down), in which the non-Abelian Maxwell equations can be written compactly as

$$\frac{1}{\tau} D_\alpha(\tau F^{\alpha\beta}) = j^\beta, \tag{3.6}$$

where indices have been raised with the inverse of the metric $g_{\alpha\beta}(\tau)$ introduced in Eq. (3.5).

Similarly to spacetime rapidity η, we define momentum-space rapidity y for the massless particles according to

$$p^\mu = p_\perp(\cosh y, \cos\phi, \sin\phi, \sinh y). \tag{3.7}$$

In comoving coordinates, this reads

$$\begin{aligned} p^\tau &= \sqrt{p_\perp^2 + \tau^2(p^\eta)^2} = \cosh\eta p^0 - \sinh\eta p^z \\ &= p_\perp \cosh(y - \eta), \end{aligned} \tag{3.8}$$

$$\begin{aligned} p^\eta &= -p_\eta/\tau^2 = (\cosh\eta p^z - \sinh\eta p^0)/\tau = p'^z/\tau \\ &= p_\perp \sinh(y - \eta)/\tau. \end{aligned} \tag{3.9}$$

[4] In the notation of Ref. [77] where $f \sim \alpha_s^{-c}$, $\tau \propto \alpha_s^{-a}$, $\xi^{1/2} \sim \delta^{-1} \equiv \alpha_s^{-d}$, our framework is located at parametric time $a = 0$ with parametric occupancy $c = 1 - \frac{\epsilon}{2}$ and parametric anisotropy $d = 0$.

[5] The relation to three-vectors is defined by $\partial_\alpha = \partial/\partial x^\alpha$ and $A^\mu = (\phi, \vec{A})$. Thus $A_\alpha = (A_\tau, -A^x, -A^y, A_\eta)$.

Instead of the standard lightlike vector $v^\mu = p^\mu/p^0$ which contains a unit three-vector and which was introduced in Eq. (3.1), we shall define

$$V^\alpha = \frac{p^\alpha}{p_\perp} = \Big(\cosh(y-\eta), \cos\phi, \sin\phi, \frac{1}{\tau}\sinh(y-\eta)\Big), \tag{3.10}$$

normalized such that it has a unit two-vector in the transverse plane.

Since

$$\begin{aligned} p^\tau \partial_\tau p_\eta(x)|_{y,\mathbf{p}_\perp} &= -p_\perp^2 \sinh(y-\eta)\cosh(y-\eta), \\ &= -p^\eta \partial_\eta p_\eta(x)|_{y,\mathbf{p}_\perp}, \end{aligned} \tag{3.11}$$

this can be solved by $f_0(\mathbf{p}, \mathbf{x}, t) = f_0(\mathbf{p}_\perp, p_\eta(x)) = f_0(\mathbf{p}_\perp, -p'^z(x)\tau(x))$. For the case of longitudinal free streaming which is isotropic at the particular proper time $\tau = \tau_{\rm iso}$ one can write f_0 in the form

$$f_0(\mathbf{p}, x) = f_{\rm iso}\left(\sqrt{p_\perp^2 + \Big(\frac{p'^z\tau}{\tau_{\rm iso}}\Big)^2}\right) = f_{\rm iso}\Big(\sqrt{p_\perp^2 + p_\eta^2/\tau_{\rm iso}^2}\Big). \tag{3.12}$$

Note that f_0 above falls into the general Romatschke-Strickland form for momentum-space anisotropic distribution functions [46].

B. Gauge-covariant Boltzmann-Vlasov equations in a longitudinally expanding plasma

In comoving coordinates the gauge-covariant Boltzmann-Vlasov equations for colored perturbations δf^a of a neutral collisionless plasma with boost-invariant background distribution f_0 read

$$V\cdot D\delta f^a|_{p^\mu} = gV^\alpha F^a_{\alpha\beta}\partial^\beta_{(p)} f_0(\mathbf{p}_\perp, p_\eta). \tag{3.13}$$

Here the derivative on the left-hand side has to be taken at fixed Cartesian p^μ rather than fixed comoving p^α. Notice also that only derivatives of $f_0(\mathbf{p}_\perp, p_\eta)$ with $\partial^\beta_{(p)}$ where the 4-index is up do not introduce explicit τ dependence so that one still has $p\cdot\partial(\partial^\beta_{(p)} f_0)|_p = p\cdot\partial(\partial^\beta_{(p)} f_0)|_p = 0$.

Equation (3.13) can be solved in terms of an auxiliary field $W_\beta(x;\phi,y)$ that does not depend on the hard scale p^0 and which is defined by

$$\delta f(x;p) = -gW_\beta(x;\phi,y)\partial^\beta_{(p)} f_0(p_\perp, p_\eta), \tag{3.14}$$

if it satisfies

$$V\cdot DW_\beta|_{\phi,y} = V^\alpha F_{\beta\alpha}. \tag{3.15}$$

Since the fluctuations δf^a give the induced current in

$$D_\mu F^{\mu\nu}_a = j^\nu_a = gt_R\int\frac{d^3p}{(2\pi)^3}\frac{p^\mu}{2p^0}\delta f_a(\mathbf{p},\mathbf{x},t), \tag{3.16}$$

j can be expressed in terms of integrals over the W fields. (Here t_R is a suitably normalized group factor, while the total number of degrees of freedom of the hard particles is contained in the normalization of the distribution function f_0.)

With (3.12) we have

$$\begin{aligned} \partial^\beta_{(p)} f_0 &= f_0'\partial^\beta_{(p)}\sqrt{p_\perp^2 + p_\eta^2/\tau_{\rm iso}^2} \\ &= f_0'\frac{\Big(0, -\cos\phi, -\sin\phi, -\frac{\tau}{\tau_{\rm iso}^2}\sinh(y-\eta)\Big)}{\sqrt{1+\frac{\tau^2}{\tau_{\rm iso}^2}\sinh^2(y-\eta)}}, \end{aligned} \tag{3.17}$$

which yields

$$\begin{aligned} j^\alpha = -\frac{m_D^2}{2}\int_0^{2\pi}\frac{d\phi}{2\pi}\int_{-\infty}^{\infty} dy V^\alpha\Big(1+\frac{\tau^2}{\tau_{\rm iso}^2}\sinh^2(y-\eta)\Big)^{-2} \\ \times \mathcal{W}(x;\phi,y), \end{aligned} \tag{3.18}$$

where

$$\begin{aligned} \mathcal{W} = V^i W_i - \frac{1}{\tau_{\rm iso}^2}V_\eta W_\eta, \qquad V^i = (\cos\phi, \sin\phi), \\ V_\eta = -\tau\sinh(y-\eta), \end{aligned} \tag{3.19}$$

and

$$m_D^2 = -g^2 t_R\int_0^\infty\frac{dp\,p^2}{(2\pi)^2}f'_{\rm iso}(p). \tag{3.20}$$

The (constant) mass parameter m_D equals the Debye mass at the proper time $\tau_{\rm iso}$.

The combination $\mathcal{W}$ introduced above satisfies

$$V\cdot D\mathcal{W} = \Big(V^i F_{i\tau} + \frac{\tau^2}{\tau_{\rm iso}^2}V^\eta F_{\eta\tau}\Big)V^\tau + V^i V^\eta F_{i\eta}\Big(1-\frac{\tau^2}{\tau_{\rm iso}^2}\Big). \tag{3.21}$$

This single equation for $\mathcal{W}$ in combination with the Yang-Mills equations and the integral giving j in terms of $\mathcal{W}$ closes our equations of motion. To solve them numerically, we adopt the comoving temporal gauge $A^\tau = 0$ and introduce canonical conjugate field momenta for the remaining gauge fields according to

$$\Pi^i = \tau\partial_\tau A_i = -\tau\partial_\tau A^i = -\Pi_i, \tag{3.22}$$

and

$$\Pi^\eta = \frac{1}{\tau}\partial_\tau A_\eta. \tag{3.23}$$

In terms of fields and conjugate momenta, the Yang-Mills equations take the form

$$\tau\partial_\tau\Pi^\eta = j_\eta - D_i F^i{}_\eta, \tag{3.24}$$

$$\tau^{-1}\partial_\tau\Pi_i = j^i - D_j F^{ji} - D_\eta F^{\eta i}, \tag{3.25}$$

while the Gauss law constraint takes the form

$$\tau j^{\tau} = D_{\eta}\Pi^{\eta} + D^{i}\Pi_{i}. \tag{3.26}$$

In temporal gauge, where $F_{i\tau} = \Pi_i/\tau$ and $F_{\eta\tau} = -\tau\Pi^{\eta}$, the field equation for $\mathcal{W}$, Eq. (3.21), becomes

$$\begin{aligned}\partial_{\tau}\mathcal{W}(\tau,\mathbf{x}_{\perp},\eta;\phi,y) &= -\frac{1}{\cosh(\bar{y})}\left[v^{i}D_{i}\mathcal{W} + \frac{\sinh(\bar{y})}{\tau}D_{\eta}\mathcal{W}\right] + \frac{1}{\tau}v^{i}\Pi_{i} \\ &\quad - \frac{\tau^{2}\sinh(\bar{y})}{\tau_{\rm iso}^{2}}\Pi^{\eta} + \frac{\tanh(\bar{y})}{\tau}\left(1-\frac{\tau^{2}}{\tau_{\rm iso}^{2}}\right)v^{i}F_{i\eta}, \\ &\quad \text{with } \bar{y} \equiv y-\eta. \end{aligned} \tag{3.27}$$

In the limit that all fields are independent of the transverse spatial directions Eqs. (3.24)–(3.27) reduce to the 1D + 3V equations of Ref. [85].

We can recast (3.27) into a form which is more convenient for computing the currents in Eq. (3.18) by defining

$$\mathcal{W}(\tau,\mathbf{x}_{\perp},\eta;\phi,y) \equiv \bar{f}(\tau,\tau_{\rm iso},\bar{y})\bar{W}(\tau,\mathbf{x}_{\perp},\eta;\phi,\bar{y}), \tag{3.28}$$

with

$$\bar{f}(\tau,\tau_{\rm iso},\bar{y}) = \left(1+\frac{\tau^{2}}{\tau_{\rm iso}^{2}}\sinh^{2}\bar{y}\right)^{2}. \tag{3.29}$$

We also replaced y by $\bar{y} \equiv y-\eta$ as argument of $\bar{W}$ because the auxiliary fields turn out to be peaked around $y \sim \eta$.

Now using

$$\partial_{\tau}\mathcal{W} = \bar{f}\partial_{\tau}\bar{W} + \frac{\partial\bar{f}}{\partial\tau}\bar{W}, \tag{3.30}$$

$$\begin{aligned}D_{\eta}\mathcal{W}(\tau,\mathbf{x}_{\perp},\eta;\phi,y) &= (D_{\eta}-\partial_{\bar{y}})[\bar{f}\,\bar{W}(\tau,\mathbf{x}_{\perp},\eta;\phi,\bar{y})] \\ &= \bar{f}(D_{\eta}-\partial_{\bar{y}})\bar{W} - \frac{\partial\bar{f}}{\partial\bar{y}}\bar{W}, \end{aligned} \tag{3.31}$$

$$D_{i}\mathcal{W} = \bar{f}D_{i}\bar{W}, \tag{3.32}$$

together with

$$\tanh\bar{y}\frac{\partial\bar{f}}{\partial\bar{y}} = \frac{\partial\bar{f}}{\partial\tau},$$

we obtain

$$\begin{aligned}\partial_{\tau}\bar{W}(\tau,\mathbf{x}_{\perp},\eta;\phi,\bar{y}) &= -\frac{1}{\cosh\bar{y}}\left[v^{i}D_{i}\bar{W} + \frac{\sinh\bar{y}}{\tau}(D_{\eta}\bar{W}-\partial_{\bar{y}}\bar{W})\right] \\ &\quad + \frac{1}{\bar{f}(\tau,\tau_{\rm iso},\bar{y})}\left[\frac{1}{\tau}v^{i}\Pi_{i} - \frac{\tau^{2}\sinh\bar{y}}{\tau_{\rm iso}^{2}}\Pi^{\eta}\right. \\ &\quad \left. + \frac{\tanh\bar{y}}{\tau}\left(1-\frac{\tau^{2}}{\tau_{\rm iso}^{2}}\right)v^{i}F_{i\eta}\right]. \end{aligned} \tag{3.33}$$

In terms of $\bar{W}(\tau,\mathbf{x}_{\perp},\eta;\phi,\bar{y})$ the expression for the current (3.18) simplifies to

$$\begin{aligned}j^{\alpha}(\tau,\mathbf{x}_{\perp},\eta) &= -\frac{m_{D}^{2}}{2}\int_{0}^{2\pi}\frac{d\phi}{2\pi}\int_{-\infty}^{\infty}d\bar{y}V^{\alpha}\bar{W}(\tau,\mathbf{x}_{\perp},\eta;\phi,\bar{y}). \end{aligned} \tag{3.34}$$

The equations of motion listed above are numerically solved by discretizing them in space and velocity space (hence the designation 3D + 3V). The gauge fields live on the three-dimensional space parametrized by spacetime rapidity η and two transverse coordinates $\mathbf{x}_{\perp}$. The $\mathcal{W}$ field lives additionally in velocity space, which because of the masslessness of the hard particles is, in the end, two-dimensional, parametrized by $\bar{y}$ and ϕ.

For the details of the lattice discretizations used we refer the reader to Appendix A.

IV. INITIAL CONDITIONS

A. Matching of the Debye mass with CGC parameters

As in our 1D + 3V simulations [85], we evolve from an initial time $\tau_0 \simeq Q_s^{-1}$ and fix the density of our initial plasma such that it matches estimates obtained from the CGC framework.

According to Ref. [90], the initial hard-gluon density can be written as

$$n(\tau_0) = c\frac{N_g Q_s^3}{4\pi^2 N_c \alpha_s(Q_s\tau_0)}, \tag{4.1}$$

with c being the gluon liberation factor, which following an analytical estimate by Kovchegov [91] we choose as $c = 2\ln 2 \approx 1.386$. While being significantly higher than the original estimates $c \simeq 0.5$ of Refs. [92,93], this value is in fact rather close to the most recent numerical result $c \simeq 1.1$ by Lappi [94].

In our effective field equations, the initial hard-gluon density enters only through the mass parameter m_D, which is defined as the Debye mass at the proper time $\tau_{\rm iso}$. In the glasma phase of the CGC framework, the pressure at early times is strongly anisotropic, with the longitudinal pressure starting out even with negative values. To model this approximately, we formally choose $\tau_{\rm iso} \ll \tau_0$, so that our initial particle distribution has initial pressure $P_L \ll P_T$. Sticking to our previous choice in Ref. [85] we take $\tau_{\rm iso} = 0.1\tau_0$. The correspondingly oblate distribution function is taken to be obtained from $f_{\rm iso}(p) = \mathcal{N}(2N_g)/(e^{p/T}-1)$, where $N_g = N_c^2 - 1$ is the number of gluons, since in CGC calculations an approximately thermal distribution was obtained for the gluon distribution in transverse directions. Following Ref. [95] we set this transverse temperature $T = Q_s/d$ with $d^{-1} \simeq 0.47$. Equation (4.1) then fixes the normalization factor $\mathcal{N}$ through

$$n(\tau_0)\frac{\tau_0}{\tau_{\rm iso}} = n(\tau_{\rm iso}) = \frac{2\zeta(3)}{\pi^2}\mathcal{N}N_g T^3. \tag{4.2}$$

In a plasma containing only gluons with distribution function $f_{\rm iso}$, the Debye mass is given by

$$m_D^2(\tau_{\rm iso}) = \mathcal{N}\frac{4\pi\alpha_s N_c T^2}{3}. \tag{4.3}$$

With $N_c = 3$ and the above values for c and d we thus obtain

$$m_D^2(\tau_{\rm iso})\tau_0^2(Q_s\tau_0)^{-1} = \frac{\pi cd}{6\zeta(3)}\frac{\tau_0}{\tau_{\rm iso}} \approx 1.285\frac{\tau_0}{\tau_{\rm iso}}. \tag{4.4}$$

In our previous studies of a stationary anisotropic plasma we have observed little difference between simulations using gauge group SU(2) versus SU(3) provided the same value of m_D was used [54,55], so we adopt the value (4.4) for our simulations with gauge group SU(2).

Notice that in the above matching which involved an overpopulated distribution function $n(\tau_0) \propto \alpha_s^{-1}$ the gauge coupling dropped out in the mass parameter m_D^2. As discussed in Sec. III, this means that we are extrapolating the hard-loop framework, which assumes a parametric separation of hard and soft scales, to its very limits. In the following we shall compare hard and soft contributions to the pressure and find that the soft field contributions are small compared to the hard particle contributions even after plasma instabilities have grown nonperturbatively strong. As long as this is the case, we assume that the hard-loop framework is still applicable.

In order to compare soft and hard contributions, we finally have to fix the gauge coupling. For that purpose we shall choose $\alpha_s = 0.3$ or $g = 1.94$ as a representative value.

B. Initial field fluctuations

In order to have seed fields for the unstable modes in an anisotropic plasma with oblate anisotropy, initial fluctuations that break perfect boost invariance are required. Fluctuations in the sources of heavy-ion collisions as well as vacuum fluctuations in all fields are inevitable, and by "natural selection" those fluctuations which lead to the most rapid onset of growth will dominate all later dynamics.

In previous hard-loop lattice simulations with fixed anisotropy the question of which initial conditions to choose was rather unimportant as long as unstable modes were excited. Seed fields in chromofields or in $\mathcal{W}$ fields were considered on the basis of convenience.

As it turns out, more care is needed in the expanding case. In Ref. [84], where the formalism of hard-expanding-loops was introduced and studied semianalytically in the (1 + 1)-dimensional Abelian case, only initial conditions formulated in terms of transverse electric fields were considered. Likewise, only seed fields in transverse chromofields were subsequently employed in the numerical 1D + 3V non-Abelian lattice study of Ref. [85], which in the weak-field regime reproduced the earlier semianalytical results, and thus also the original finding of an (with regard to heavy-ion collisions) uncomfortably long delay of the onset of growth of plasma instabilities. (The generalization considered in Ref. [85], namely to also initialize magnetic fields, did not change this conclusion.)

In Ref. [86] the semianalytical treatment of Ref. [84] was generalized to the much more complex case of generic (3 + 1)-dimensional Abelian modes in an expanding plasma, and at this occasion also the most general initial conditions were considered, involving both electric and magnetic fields as well as the auxiliary $\mathcal{W}$ fields which describe fluctuations in the induced currents. Surprisingly enough, initial fluctuations in the $\mathcal{W}$ fields lead to a drastic (order-of-magnitude) reduction of the initial delay of the onset of growth. Evidently, initial conditions in the electric and magnetic fields predominantly give stable plasmon modes and less strongly excite the unstable modes. The latter are instead more easily triggered by fluctuations in the induced currents described by the $\mathcal{W}$ fields.

The simplest initial conditions that provide seed fields for Weibel instabilities while having initial vanishing charge density are ϕ- and y-independent fluctuations of the component fields $W_i(x;\phi,y)$ and $W_\eta(x;\phi,y)$. The former induce transverse currents which are most directly related to the α modes, whereas a ϕ- and y-independent W_η seeds longitudinal currents that are less important for the plasma instabilities. Because of their subdominant effect, we have mostly omitted W_η seeds and only kept $W_i(x;\phi,y)$ when assembling the initial $\mathcal{W}$ field.

Another point to consider is the spectrum of initial fluctuations. Because we are using highly anisotropic lattices with particularly fine resolution in the longitudinal direction, initializing with white noise fluctuations would correspond to very high UV noise in longitudinal wave numbers. We have therefore implemented an adjustable mode number cutoff, Λ_ν, in wave numbers ν dual to the rapidity variable η and populate all modes $\propto e^{i\nu\eta}$ equally below this cutoff, with white noise in transverse directions. Because the "natural selection" of plasma instabilities quickly picks out the most strongly growing modes, we have refrained from attempts to model the initial spectrum other than ensuring that a good range of seeds is available.

V. OBSERVABLES

Here we list the quantities which we will present in the results section. We present only the continuum formulas. For the details of the lattice discretizations used we refer the reader to Appendix A. Note that in most of the results presented we have averaged observables over a set of runs in order to account for variations in the random initial conditions employed.

A. Field energy densities and pressures

The transverse/longitudinal electric and magnetic components of the field energy density are given by

$$\begin{aligned}\mathcal{E} &= \mathcal{E}_T + \mathcal{E}_L = \mathcal{E}_{B_T} + \mathcal{E}_{E_T} + \mathcal{E}_{B_L} + \mathcal{E}_{E_L} \\ &= \mathrm{tr}[\tau^{-2}F_{\eta i}^2 + \tau^{-2}\Pi_i^2 + F_{xy}^2 + (\Pi^\eta)^2],\end{aligned} \tag{5.1}$$

and the Hamiltonian density is given by $\mathcal{H} = \tau\mathcal{E}$. The transverse and longitudinal field pressures are obtained via

$$\mathcal{P}_L^{\text{field}} = \mathcal{E}_T - \mathcal{E}_L, \tag{5.2}$$

$$\mathcal{P}_T^{\text{field}} = \mathcal{E}_L. \tag{5.3}$$

Note that from the above, one has at all times $2\mathcal{P}_T^{\text{field}} + \mathcal{P}_L^{\text{field}} = \mathcal{E}$ such that the energy-momentum tensor is traceless.

B. Particle pressures

In a comoving frame, the energy density and pressure components of the hard particle background can be determined by evaluating

$$T^{\alpha\beta}_{\text{part}} = (2\pi)^{-3} \int d^2p_T dy p^\alpha p^\beta f_0, \tag{5.4}$$

which yields

$$\mathcal{E}_{\text{part}}(\tau) = T^{\tau\tau}_{\text{part}} = \frac{1}{2}\left[\frac{1}{\bar{\tau}^2} + \frac{\arcsin\sqrt{1-\bar{\tau}^{-2}}}{\sqrt{\bar{\tau}^2-1}}\right]\mathcal{E}_{\text{iso}}, \tag{5.5}$$

$$\begin{aligned}\mathcal{P}_T^{\text{part}}(\tau) &= \frac{1}{2}T^{ii}_{\text{part}} \\ &= \frac{1}{4(\bar{\tau}^2-1)}\left[1 + \frac{\bar{\tau}^2-2}{\sqrt{\bar{\tau}^2-1}}\arcsin\sqrt{1-\bar{\tau}^{-2}}\right]\mathcal{E}_{\text{iso}},\end{aligned} \tag{5.6}$$

$$\begin{aligned}\mathcal{P}_L^{\text{part}}(\tau) &= -T^{\eta}_{\text{part}\,\eta} \\ &= \frac{1}{2(\bar{\tau}^2-1)}\left[-\frac{1}{\bar{\tau}^2} + \frac{\arcsin\sqrt{1-\bar{\tau}^{-2}}}{\sqrt{\bar{\tau}^2-1}}\right]\mathcal{E}_{\text{iso}},\end{aligned} \tag{5.7}$$

where $\mathcal{E}_{\text{iso}} = \mathcal{E}_{\text{part}}(\tau_{\text{iso}})$, $\bar{\tau} \equiv \tau/\tau_{\text{iso}}$ and we have assumed $\bar{\tau} \geq 1$.

In the results section as a measure of isotropization we will present plots of the ratio

$$\frac{\mathcal{P}_L}{\mathcal{P}_T} = \frac{\mathcal{P}_L^{\text{field}} + \mathcal{P}_L^{\text{part}}}{\mathcal{P}_T^{\text{field}} + \mathcal{P}_T^{\text{part}}}. \tag{5.8}$$

If this quantity is less that 1, then the system possesses an overall oblate momentum-space anisotropy and if it is greater than 1, then it possesses a prolate momentum-space anisotropy.

C. Energy spectra

In order extract spectral information about the field configurations, the canonical way to proceed is to gauge fix to a spatially smooth gauge such as Coulomb gauge and then extract mode occupation numbers from either the electric or magnetic fields [58,96,97]. However, such a method is not free from ambiguity in the infrared due to the lingering problem of large gauge transformations (aka Gribov copies).

Here we follow a different method introduced by Fukushima and Gelis [82] in which we extract the electric and magnetic fields at a given proper time from the lattice simulation using

$$\begin{aligned}
E_i(\mathbf{x}_T, \eta) &= \tau^{-1}\Pi_i, \\
E_L(\mathbf{x}_T, \eta) &= \Pi^\eta, \\
B_x(\mathbf{x}_T, \eta) &= F_{\eta y} \simeq \frac{2}{iga_\eta\tau}\,\text{tr}[t^a(1-U_{\eta y})], \\
B_y(\mathbf{x}_T, \eta) &= F_{\eta x} \simeq \frac{2}{iga_\eta\tau}\,\text{tr}[t^a(1-U_{\eta x})], \\
B_L(\mathbf{x}_T, \eta) &= F_{xy} \simeq \frac{2}{ig}\,\text{tr}[t^a(1-U_{xy})].
\end{aligned} \tag{5.9}$$

We then perform a three-dimensional Fourier transform of each field component, e.g.,

$$E_i(\mathbf{k_T}, \nu) = \int \frac{d^2x_T}{(2\pi)^2}\frac{d\eta}{2\pi}E_i(\mathbf{x_T}, \eta)e^{i\mathbf{k}_T\cdot\mathbf{x}_T}e^{i\nu\eta}. \tag{5.10}$$

Since we are primarily interested in the longitudinal spectra, we integrate over the transverse wave vectors to obtain, e.g.,

$$E_i(\nu) = \int \frac{d^2k_T}{(2\pi)^2}E_i(\mathbf{k_T}, \nu).$$

Having obtained the field components we can decompose the energy density in terms of the longitudinal wave number

$$\begin{aligned}
\mathcal{E}_E &= \int \frac{d\nu}{2\pi}\mathcal{E}_E(\nu) = \int \frac{d\nu}{2\pi}[\mathcal{E}_{E_L}(\nu) + \mathcal{E}_{E_T}(\nu)], \\
\mathcal{E}_B &= \int \frac{d\nu}{2\pi}\mathcal{E}_B(\nu) = \int \frac{d\nu}{2\pi}[\mathcal{E}_{B_L}(\nu) + \mathcal{E}_{B_T}(\nu)],
\end{aligned} \tag{5.11}$$

where we have the energy density at each longitudinal wave number

$$\begin{aligned}
\mathcal{E}_{E_L}(\nu) &= \text{tr}[E_L(-\nu)E_L(\nu)] = \text{tr}|E_L|^2, \\
\mathcal{E}_{E_T}(\nu) &= \sum_{i\in\{x,y\}}\text{tr}[E^i(-\nu)E^i(\nu)] = \sum_{i\in\{x,y\}}\text{tr}|E^i|^2, \\
\mathcal{E}_{B_L}(\nu) &= \text{tr}[B_L(-\nu)B_L(\nu)] = \text{tr}|B_L|^2, \\
\mathcal{E}_{B_T}(\nu) &= \sum_{i\in\{x,y\}}\text{tr}[B^i(-\nu)B^i(\nu)] = \sum_{i\in\{x,y\}}\text{tr}|B^i|^2,
\end{aligned} \tag{5.12}$$

where the traces are color traces. The total longitudinal energy spectra are obtained by summing all components

$$\mathcal{E}(\nu) = \mathcal{E}_{E_L}(\nu) + \mathcal{E}_{E_T}(\nu) + \mathcal{E}_{B_L}(\nu) + \mathcal{E}_{B_T}(\nu). \tag{5.13}$$

The spectral decomposition (5.12) is not gauge invariant; gauge transformations could in principle still redistribute the energy distribution in ν, but this redistribution is limited by the fact that the integrals (5.11) are gauge invariant. We thus expect that the degree of gauge dependence is much milder than in bare mode occupation numbers of the gauge fields before they are made maximally smooth by going to Coulomb gauge.

Note that one can compute the total energy density via Eqs. (5.1) and (5.11) and compare as a cross-check of the spectra calculation. Numerically we find very good agreement between the two methods. We have also performed a Fourier analysis of the spatial distribution of the (gauge-invariant) chromofield energy on the lattice. Besides the expected peak at zero momentum, we found that the remaining spatial fluctuations reflect closely the spectral decomposition defined through Eq. (5.12).

VI. RESULTS

In this section we present the results of our numerical simulations for SU(2) gauge fields which include real-time gauge field energy densities, particle and field pressures, energy spectra, and fit to the energy spectra. For all results shown in this section we initialize current fluctuations (via $\mathcal{W}$ fields) with an amplitude Δ as described in Sec. IV and Appendix C. In order to generate occupation numbers $\sim 1/2$ consistent with those expected from initial quantum-mechanical rapidity fluctuations [80] one should choose $\Delta \sim 1.6$. Unfortunately, due to numerical limitations stemming from the fact that we simulate compact gauge groups, we are unable to use such a large value of Δ. Instead in the main plots shown below we use an initial current fluctuation amplitude of $\Delta = 0.8$ which can be expected to result in longer isotropization times than one would obtain with the larger seed values necessary. In order to assess the dependence of our results on Δ we present the variation of the energy density and pressure ratio. In the conclusions we will discuss the extrapolation of our result to realistic values of Δ.

For all results shown the lattice spatial size was $N_T^2 \times N_\eta = 40^2 \times 128$ with transverse lattice spacing of $a = Q_s^{-1}$ and longitudinal lattice spacing of $a_\eta = 0.025$. The lattice size in velocity space was $N_u \times N_\phi = 128 \times 32$. The longitudinal spectral cutoff for the current-based rapidity fluctuations was taken to be $\Lambda_\nu \nu_{\min} = 8\nu_{\min} \approx 15.7$. The initial time was taken to be $\tau_0 = Q_s^{-1}$ and we used $\tau_{\rm iso}/\tau_0 = 0.1$. For the temporal time step we use $\epsilon = 10^{-2}\tau_0$. For details of the lattice discretizations used for the equations of motion we refer the reader to Appendix A. When plotting observables as a function of time we will plot them as a function of $\tilde{\tau} \equiv Q_s \tau/10$. For LHC one has $Q_s \simeq 2$ GeV $= (0.1$ fm$)^{-1}$ and for RHIC one has $Q_s \simeq 1.4$ GeV $= (0.14$ fm$)^{-1}$. The division by a factor of 10 makes it so that when considering LHC energies each interval of $\Delta\tilde{\tau} = 1$ is 1 fm/c. At RHIC each interval of $\Delta\tilde{\tau} = 1$ is 1.4 fm/c.

For numerical tests such as varying the lattice spacing, lattice size, spectral cutoffs, and velocity resolution we refer the reader to Appendix D. The lattice equations of motion are written in terms of rescaled dimensionless fields. When comparing pressures in soft fields with pressures from hard particles, we have assumed a value of $g = 1.94$ consistent with $\alpha_s = 0.3$ which is in the right ballpark for RHIC and LHC heavy-ion collisions. Note that formally our results are only trustable in the weak-coupling limit and we are making a bold extrapolation when we assume $\alpha_s = 0.3$. Nevertheless, we do this in order to obtain a rough estimate of the isotropization time associated with the chromo-Weibel instability in a background which is undergoing longitudinal free streaming expansion.

A. Energy densities

In Fig. 3 we show the chromoelectric, chromomagnetic, and total energy densities (5.1) as a function of proper time. The results shown are averaged over 50 runs which will serve as our standard set of runs for most observables in this section.[6] From Fig. 3 we see that for the first $\tilde{\tau} \lesssim 1.2$ the soft fields are depleted by the longitudinal expansion. After this time the unstable modes present in the initial condition begin to show appreciable growth. Initially all components of the chromofield start out with approximately equal energy density, but at this time the system begins to be dominated by transverse chromomagnetic fields. However, due to the large amplitude of the initial current fluctuations we quickly see the development of large transverse chromoelectric fields followed by rapid growth in the longitudinal chromoelectric and chromomagnetic fields.

All field components become approximately the same magnitude at a time of $\tilde{\tau} \sim 3.5$ when $\Delta = 0.8$. We will refer to the point in time at which all components of the field energy density give approximately the same contribution as the "non-Abelian point." From this point on, in contrast to the fixed-anisotropy simulations, one does not see a saturation of the exponential growth, just a moderate reduction of the growth rate. Instead we see that, similar to the 1D + 3V simulations, the transverse chromoelectric and chromomagnetic fields begin to dominate the energy density and do so for the rest of the simulation. As we will see below, by the end of the simulation a large portion of the energy is in ultraviolet longitudinal lattice modes and one starts to see lattice artifacts; however, up to this point we see no sign of saturation of the roughly exponential growth in the chromofields.

In Fig. 4 we show the total field energy density for different initial current fluctuation amplitudes $\Delta \in \{0.1, 0.2, 0.4, 0.8\}$. As can be seen from this figure, apart from a slight reduction in unstable mode growth when the fields reach the non-Abelian point (which moves to large times for smaller Δ), the behavior is qualitatively independent of the assumed amplitude. We note that there is a fundamental limit on how large one can make Δ without violating the assumptions of the hard-loop effective theory

[6] In Appendix D Fig. 12(a) we plot the total field energy density resulting from all 50 runs for comparison.

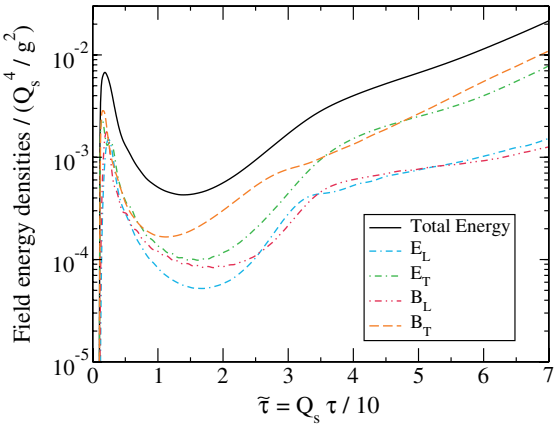

FIG. 3 (color online). Chromoelectric, chromomagnetic, and total energy densities (5.1) as a function of proper time from averaging over our standard set of runs. Proper time is normalized such that when using $Q_s = 2$ GeV each unit of $\Delta\tilde{\tau}$ is 1 fm/c. See text for simulation parameters used.

we employ. In practice, this limit is set by the physical requirement that the majority of the energy density should still be contained in the hard particle distribution function. We note that for $\Delta = 0.8$ we are still safely below this bound with the initially induced soft fields only carrying only $\sim$1.5% of the total energy with the vast majority of the energy coming from the hard sector.

B. Pressures

In Fig. 5 we show the hard particle and field pressures scaled by $\tau_0^3\tau$ as a function of proper time. The data were taken from the same set of runs as Fig. 3 and the pressures were computed using Eq. (5.3). The scaling chosen in this figure renders the vertical axis dimensionless and has the added benefit of making the scaled hard particle transverse pressure constant for better visualization.

As can be seen from Fig. 5 the system is initially highly anisotropic with the transverse particle pressure dominating all other contributions. The τ-scaled longitudinal particle pressure drops like $1/\tau^2$. Note that at early times the field component of the longitudinal pressure can become negative as evidenced by Fig. 5. This is consistent with the finding of others [82] and is a result of coherent field modes. Without the unstable field growth, the system would continue to become more and more anisotropic as time progresses and continue to experience positive and negative pressure oscillations. However, as Fig. 5 demonstrates, unstable field modes begin to generate a growing longitudinal field pressure that at late times dominates all other pressure components.

It should be noted, however, that by the time the longitudinal field pressure becomes of the same magnitude as the transverse particle pressure one already expects to see a significant amount of backreaction of the hard particles on the unstable chromofields. Physically this should result in a saturation of the field pressure growth due to energy conservation. In addition, the backreaction would serve to isotropize the particle sector. Such a physical saturation is, unfortunately, not describable in the hard-loop framework since in this framework the hard particles act as an energy reservoir that can continue to pump energy into the soft sector indefinitely. Sans this caveat, we believe that this result shows evidence that the chromo-Weibel instability can restore isotropy on the fm/c time scale.

In Fig. 6 we show the total longitudinal pressure over the total transverse pressure (5.8) as a function of proper time. The data were taken from the same set of runs as Fig. 3. This plot condenses the information seen in the previous plot allowing one to easily see the point at which the plasma becomes isotropic in momentum space. As can be seen from this figure this occurs at approximately $\tilde{\tau} = 6.5$; however, the system continues to evolve beyond this point with the total longitudinal pressure then exceeding

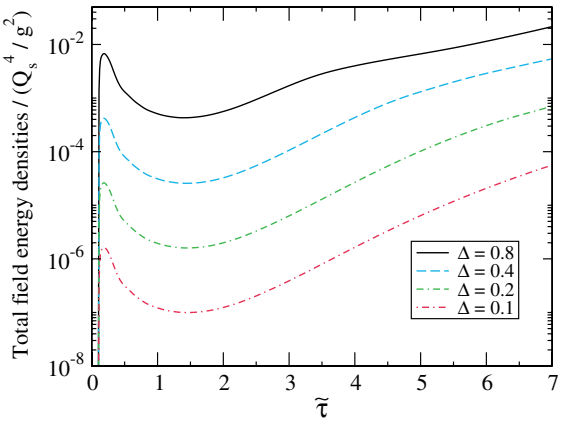

FIG. 4 (color online). Total field energy density for different initial current fluctuation magnitudes $\Delta \in \{0.1, 0.2, 0.4, 0.8\}$. See text for simulation parameters used.

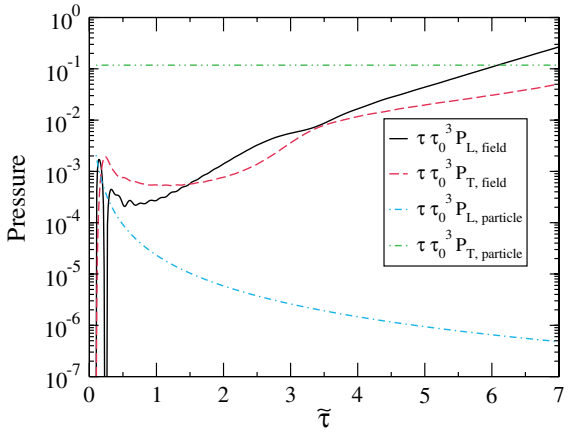

FIG. 5 (color online). Hard particle and field pressures scaled by $\tau_0^3\tau$ as a function of proper time. The data were taken from the same set of runs as Fig. 3.

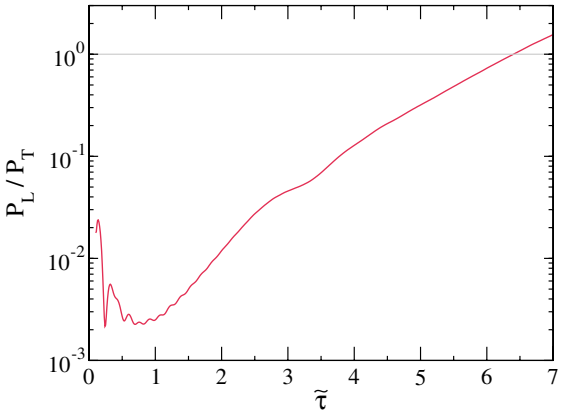

FIG. 6 (color online). Total longitudinal pressure over the total transverse pressure as a function of proper time. The data were taken from the same set of runs as Fig. 3.

the total transverse pressure. This is most definitely an artifact due to the lack of the backreaction of the hard particles on the chromofields. Therefore, we are only fully confident in the results we obtain at earlier times.

In Fig. 7 we show the total longitudinal pressure over the total transverse pressure (5.8) as a function of proper time for different initial current fluctuation magnitudes $\Delta \in \{0.1, 0.2, 0.4, 0.8\}$. The data were taken from the same runs as shown in Fig. 4. The purpose of this figure is to show that the variable which has the biggest effect on the isotropization time is our assumed magnitude of the initial current fluctuations, Δ. From this figure we see that the isotropization time scale depends roughly logarithmically on Δ. In the limit of parametrically small Δ, where the evolution is dominated by the Abelian behavior, one can infer from the analytical results of Ref. [84] that the square root of the apparent isotropization time depends linearly on $\log\Delta^{-1}$ [which would lead to the estimate of $(\log g^{-1})^2$ for the parametric dependence of isotropization time on g in the limit of weak coupling].

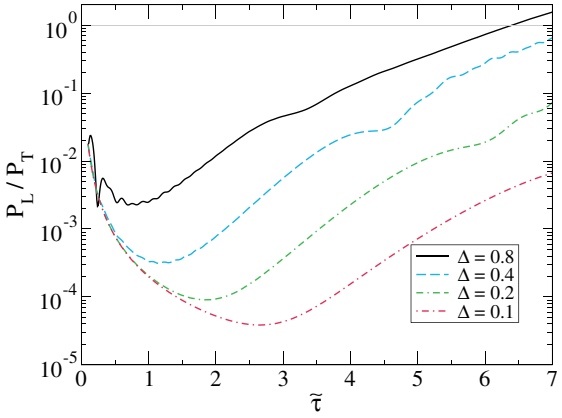

FIG. 7 (color online). Total longitudinal pressure over the total transverse pressure as a function of proper time for different initial current fluctuation magnitudes $\Delta \in \{0.1, 0.2, 0.4, 0.8\}$. The data were taken from the same runs as shown in Fig. 4.

C. Energy spectra

In Fig. 8 we show the run-averaged longitudinal energy spectra obtained via (5.13) at different proper times as a function of (a) the longitudinal wave number ν and (b) the longitudinal momentum $k_z = \nu/\tau$. The data for both plots were taken from the same set of runs as Fig. 3. In both figures the vertical axis is logarithmic while the horizontal axis is linear. From Fig. 8(a) we see the rapid emergence of an exponential distribution of longitudinal energy. The exponential spectra persist during the entire evolution. In Fig. 8(b) we show the spectra as function of the physical momentum so that one can now see the effect of the redshifting of the longitudinal momentum with time. In addition, from this figure we can easily determine a kind of effective longitudinal temperature which can be extracted from the slopes of the curves. Below we will define a fit function and extract the longitudinal temperature as a function of proper time.

Note that the emergence of this exponential spectrum is not solely due to the widening unstable mode band. Instead

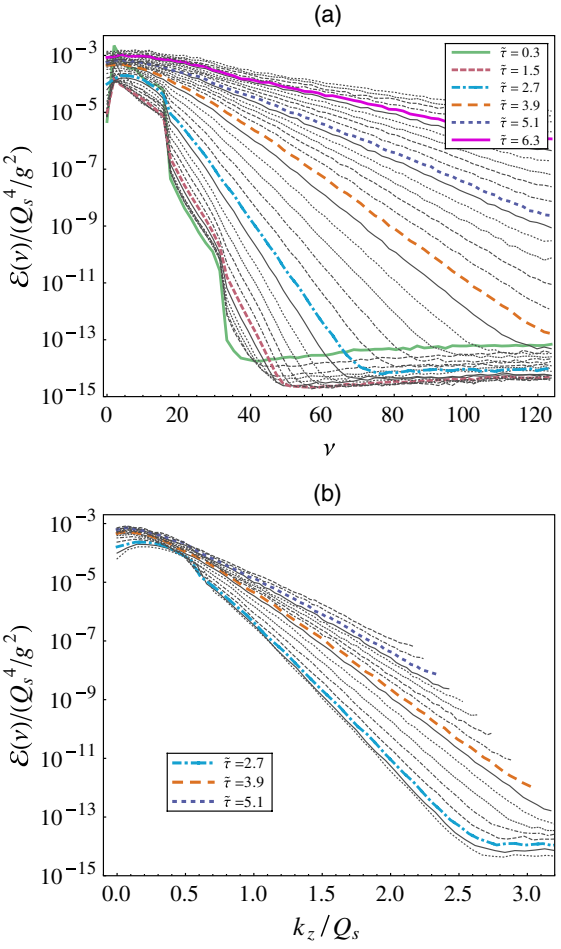

FIG. 8 (color online). The longitudinal energy spectra at various proper times as a function of (a) ν and (b) $k_z = \nu/\tau$. Data taken from the averaged runs shown in Fig. 3.

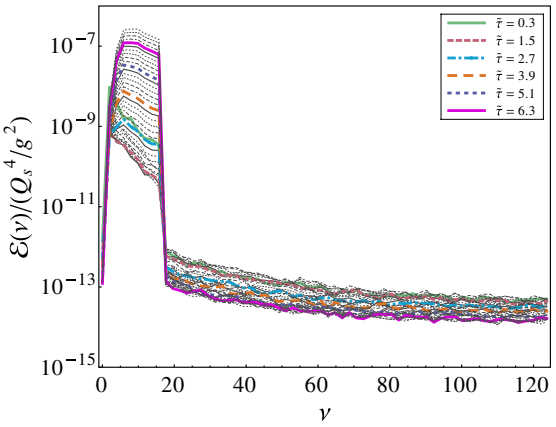

FIG. 9 (color online). The longitudinal energy spectra at various proper times as a function of ν for Abelian runs. For this figure the spectra from 40 runs were averaged.

having nonlinear mode-mode coupling is vitally important in order to populate high momentum modes which are rapidly becoming unstable as time progresses. In order to illustrate this point in Fig. 9 we show the corresponding spectra from Abelian runs. The lattice size for these Abelian runs were exactly the same as for the corresponding non-Abelian run shown in Fig. 8; however, we chose a smaller value of Δ in order to eliminate the possibility of artificial nonlinearities due to the fact that we are simulating compact $U(1)$. As we can see from this figure, only modes present in the initial conditions are amplified in the Abelian case, hence demonstrating that the emergence of an exponential longitudinal energy spectrum is intrinsically non-Abelian (nonlinear).

At first sight our exponential distribution of longitudinal energy seems to be different than the result obtained by Fukushima and Gelis who saw the emergence of a power-law spectrum in Yang-Mills solutions in an expanding QGP [82]; however, we note, importantly, that they saw the emergence of a power-law longitudinal energy spectrum only at extremely late times corresponding to $\tilde{\tau} \gtrsim 150$. At early times, their spectra also appear consistent with an exponential distribution of longitudinal energy. Since we do not include the backreaction, we are unable to comment on the asymptotic behavior of the spectra since we currently see no evidence of soft-scale saturation of the unstable mode growth. In addition, power law scaling usually emerges in the infrared and, in that sense, we are limited due to small lattices.

In Fig. 10 we show fits to spectra shown in Fig. 8(b) at several different proper times. For the fit function we assumed that the spectra corresponded to the energy density obtained from a massless Boltzmann distribution that has been integrated over transverse momenta

$$\mathcal{E} \propto \int dk_z d^2k_T \sqrt{k_T^2 + k_z^2}\, \exp\left(-\sqrt{k_T^2 + k_z^2}/T\right),$$
$$\propto \int dk_z (k_z^2 + 2|k_z|T + 2T^2) \exp(-|k_z|/T). \quad (6.1)$$

The integrand in the above expression was taken as our fit function

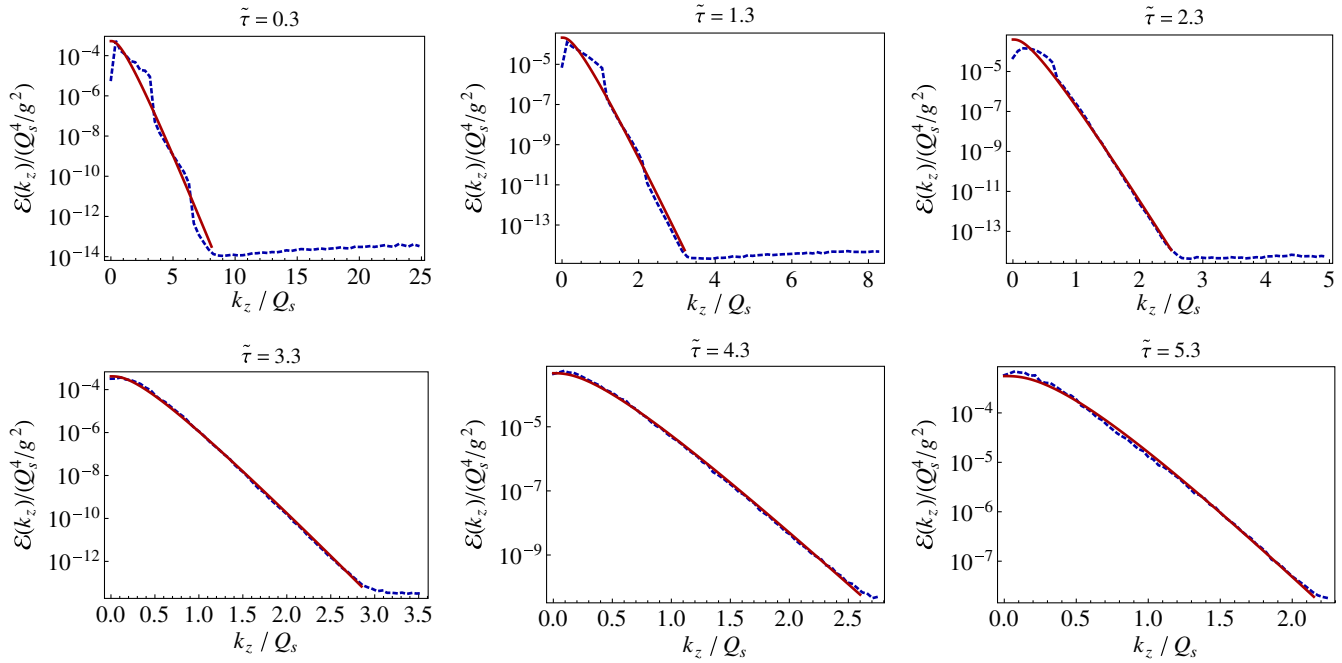

FIG. 10 (color online). Comparison of the longitudinal spectra data from Fig. 8 with fits (full lines) using the fit function (6.2) at six different proper times.

$$\mathcal{E}_{\rm fit}(k_z) = A(k_z^2 + 2|k_z|T + 2T^2)\exp(-|k_z|/T), \quad (6.2)$$

where we have allowed for an overall multiplicative constant A. At each proper time we fit the two parameters A and T; however, at early times we manually exclude regions of the spectra that are part of the ''noisy plateau'' at high longitudinal momenta, e.g., $k_z \gtrsim 8Q_s$ from the $\tilde{\tau} = 0.3$ panel shown in Fig. 10 are excluded from the fit data.

As can be seen from Fig. 10 we see evidence of a very rapid emergence of a Boltzmann longitudinal energy spectrum. At $\tilde{\tau} = 0.3$ the fit is already working quite well with the bumps seen in the spectra being nonlinear resonance ''copies'' of the initial theta-function-like distribution of longitudinal energy. By $\tilde{\tau} = 2.3$ virtually all information about the initial condition is gone and by $\tilde{\tau} = 3.3$ the system seems to exhibit an exceptional degree of longitudinal thermalization with all information about the initial condition lost. We only show six specific times in Fig. 10; however, at all simulation times $\tilde{\tau} \gtrsim 0.3$ the fits seem to work remarkably well. We note, importantly, that although the spectra shown in Fig. 10 are averaged over runs, one sees the emergence of such a Boltzmann spectrum on a run-by-run basis. We have averaged over runs in order to remove statistical noise and improve the quality of the fits.

In Fig. 11 we show the extracted fit temperatures using (6.2) as a function of proper time. We see from this figure that at early times the soft sector cools down due to longitudinal expansion, but once the instability begins to grow, the soft sector begins to heat up. We note in this context that the hard particle distribution is highly anisotropic, making it hard to associate a temperature with. The transverse temperature given by $p_{\rm hard} \sim Q_s$ is a constant for longitudinal free streaming; however, one can associate a kind of isotropic temperature by computing the fourth root of the energy density $\mathcal{E} = \mathcal{R}(\xi)\mathcal{E}_{\rm iso}(p_{\rm hard})$ [34]. One finds at late times ($\tau \gg \tau_{\rm iso}$) that $\mathcal{E} \sim \tau^{-1}$ so that $T_{\rm eff,hard} \sim \mathcal{E}^{1/4} \sim \tau^{-1/4}$ which decreases less quickly than ideal hydrodynamical behavior for which one has $T \sim \tau^{-1/3}$.

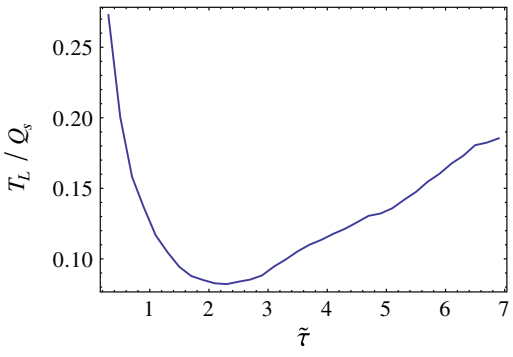

FIG. 11 (color online). The time-dependent longitudinal temperature extracted from the data contained in Fig. 8 using the fit function (6.2).

Since the hard particles still dominate the energy density, the combined soft plus hard effective temperature still decreases in time.

VII. CONCLUSIONS

In this paper we have studied the dynamics of the chromo-Weibel plasma instability in a longitudinally expanding plasma by numerically solving the full 3D + 3V real-time evolution of the hard-loop equations of motion. We utilized current fluctuations as the initial condition so that the initial fields were self-consistently triggered by the hard particles. We had three important findings: (1) there is no saturation of the chromo-Weibel instability at the ''soft scale'' on timescales relevant for heavy-ion collisions, (2) the dominant transverse chromomagnetic fields generate a rapidly growing longitudinal pressure that works to isotropize the system on time scales relevant for heavy-ion collisions, and (3) in the process of evolution the longitudinal energy spectrum shows no signs of a power-law spectrum associated with Kolmogorov turbulence, but instead shows evidence for rapid longitudinal thermalization of the gauge fields.

The finding that there is no soft-scale saturation of the plasma instability is important since this means that on the time scales relevant for heavy-ion collisions the backreaction of the hard degrees of freedom could be important. This suggests that it will be of the utmost importance to make an in-depth study of the dynamics of an unstable expanding plasma using classical Yang-Mills and Boltzmann-Vlasov simulations. However, care will have to be taken to make sure that these simulations can properly describe the soft collective modes of the system consistent with hard-loop dynamics in the high temperature limit. The fact that we do not witness soft-scale saturation of the chromo-Weibel instability is consistent with previous analyses of plasmas possessing a fixed high-magnitude momentum-space anisotropy [59,60]. In the case of HEL, the redshifting of the longitudinal momentum causes transverse unstable modes to become more and more stable as a function of time, while purely longitudinal modes continue to grow. We cannot rule out a very late time saturation on time scales far beyond what we have studied; however, such large time scales are probably not relevant to understanding thermalization of a QGP generated in heavy-ion collisions.

Our second finding concerned plasma isotropization. Extrapolating our results to conditions expected for heavy-ion collisions at the LHC, we found that for the assumed magnitude of current fluctuations, $\Delta = 0.8$, isotropization within our framework occurs at $\sim$6.5 fm/c. Further extrapolating our numerical results to $\Delta = 1.6$ which is required in order to achieve occupation numbers consistent with quantum fluctuations, one finds isotropization times on the order of 5 fm/c. However, it should be noted that we have not included the backreaction of the

hard particles on the soft background field. It is likely that the backreaction slows down the process of isotropization at late times and, therefore, the numbers quoted above should perhaps be taken as a lower bound on the time of *complete* isotropization.

We note that although the early indications from ideal hydrodynamics would imply that this time scale is much too long, in recent years it has emerged that there is very little experimental constraint on the degree of local momentum-space anisotropy in the quark gluon plasma. In HEL the precise time scale for isotropization depends on the choice of the amplitude of the initial current fluctuations and as a consequence the amplitude of the soft gauge fields at early times. We have chosen the magnitude of these fluctuations based on studies of the breaking of boost invariance in the glasma by quantum fluctuations. Of course, one can shorten the isotropization time by increasing the magnitude of the initial fluctuations used; however, within the hard-expanding-loop framework one runs the risk of violating the assumption that the energy of the system is dominated by the hard degrees of freedom. Once again this imposes a limit on what can be achieved through hard-loop simulations and calls for more comprehensive methods to tackle the problem which can properly include the backreaction.

Our final finding concerned the induced spectrum of the unstable soft modes. We found a Boltzmann distribution of longitudinal energies instead of a power law distribution as was found in static simulations. Extrapolating to RHIC and LHC conditions, this result seems to imply that one can achieve longitudinal thermalization of the quark gluon plasma on time scales of 1 fm/c. Early color glass condensate simulations demonstrated that the initial gauge field configurations were transversally thermal [98] and our results indicate that the system also quickly becomes thermal in the longitudinal direction.

The longitudinal thermalization we see is particular to non-Abelian gauge theories. In general, there are two effects occurring: (1) mode amplification due to plasma instability and (2) mode-mode coupling due to nonlinear interactions. In an Abelian plasma only mode amplification occurs and one does not see the emergence of a longitudinally thermalized spectrum. One needs the mode-mode coupling to spread the deposited energy across large ranges of momenta quickly. In the non-Abelian case, we have checked different lattice sizes, lattice spacing, etc. and the rapid emergence of a longitudinally thermalized spectrum seems to be quite robust.

We note that our finding of an exponential longitudinal energy spectrum is not in contradiction with the pure Yang-Mills simulations of Ref. [82] which found the emergence of a power-law spectrum, since the power-law spectrum observed therein only emerged at quite late times, $\tau \gtrsim 150$ fm/c. At early times Ref. [82] also found what appears to be an exponential distribution in the longitudinal energy spectrum. We also note that usually one sees power-law spectra energy in the infrared. Due to having to use many auxiliary fields we were limited to $40^2 \times 128$ lattices. In the future we plan runs on larger lattices in order to more carefully determine the infrared part of the spectrum.

Our study, however, is not without caveats. In order to have a tractable way to treat the time-dependent hard particles, we approximated them as a longitudinally free streaming ensemble. This is an extreme assumption that should be relaxed, if possible, in the future. Some work along this direction has been started in Ref. [99] where the authors were able to derive an evolution equation for a stable uniform chromoelectric field in an arbitrary time-evolving anisotropic background. It would be very interesting to see if the method employed in Ref. [99] can be extended to the entire stable and unstable mode spectrum. This caveat aside, it is interesting that even with such an extreme particle pressure anisotropy being developed, the chromo-Weibel instability is able to isotropize the system on time scales relevant for heavy-ion collisions.

The second important caveat is that we did not include the effect of the backreaction of the hard particles on the unstable soft gauge fields. Our results seem to indicate that the fields grow unabated until there will be a significant backreaction. Of course, as soon as the field amplitudes become large enough for any backreaction to occur, it is possible that this could reduce the anisotropy of the hard particles and reduce the rate of growth of the unstable soft modes.

In the context of our numerical results, the observation of continued unstable mode growth places an upper limit on the amount of time over which we can trust our hard-loop simulations; however, we find that assuming that the initial fraction of the energy carried by soft fields is small compared to the hard scale there is a window of time over which we can reliably simulate the dynamics. Our results indicate a very fast path to isotropization within this window of reliability. Addressing the question of the late time dynamics of the system is not possible within this framework[7]; however, our study might serve as a benchmark for future simulations that include backreaction in an expanding plasma.

In the future one might use hard-loop simulations to study the early time dynamics of the quark gluon plasma and the role unstable modes play. One can address interesting phenomenological questions such as measuring the shear viscosity due to plasma instabilities and studying particle transport properties such as energy loss and

[7]In this paper, we have concentrated on the phenomenology of unstable modes in a longitudinally free streaming background. For an in-depth analysis of the path to isotropy in the asymptotically small coupling limit, including late time dynamics, we refer the reader to Refs. [76,77] where parametric estimates have been made.

momentum-space diffusion. In addition, the momentum-space anisotropy dependence of many important heavy-ion collision observables such as jet energy loss, photon production, dilepton production, heavy quark energy loss, heavy quarkonium suppression, etc. have been computed [71,100–115]. It would, therefore, be interesting to study the effect of our time-dependent evolution on these observables as a possible signature of the plasma instability in heavy-ion collisions.

We note that there are now many groups studying the thermalization, isotropization, and anisotropic signatures of the quark gluon plasma in the strong coupling limit using the AdS/CFT correspondence [29–31,116–128]. It would be interesting to compare and contrast the predictions for experimental observables coming from the weakly coupled and strongly coupled frameworks.

Finally, there have also been some recent studies that have suggested that there is an inverse particle number cascade leading to Bose-Einstein condensation of soft gauge fields [129–131]. How a long-lived condensate can emerge in a non-Abelian gauge is an open question. Based on our results it is hard to judge whether this possibility is borne out, since we do not directly obtain the particle number spectra but instead the energy spectra. Determining the nature of the low momentum number spectra is complicated by gauge invariance issues; however, measurements of this spectra in fixed-anisotropy hard-loop simulations [55,57,61] and pure Yang-Mills with high occupancy [131–133] have so far shown no evidence of occupation numbers exceeding $f \sim 1/\alpha_s$ at late times. That being said it would be interesting to see if a time-evolving condensate, perhaps in the form of an overpopulated condensate of plasmons (chromoelectric oscillations), could play a role in QGP thermalization and isotropization.

ACKNOWLEDGMENTS

We would like to thank J. Berges, K. Fukushima, F. Gelis, A. Ipp, A. Kurkela, G. D. Moore, and A. Mueller for useful discussions. We thank the Vienna Scientific Cluster for providing computational resources under Project No. 70061. M. A. was supported by the Austrian Science Fund (FWF) Grants No. P19526 and No. P22114, the START Project No. Y435-N16, and the Austrian Marshall Plan Foundation. M. S. was supported by NSF Grant No. PHY-1068765 and the Helmholtz International Center for FAIR LOEWE program.

APPENDIX A: LATTICE EQUATIONS OF MOTION

In this appendix we introduce the dimensionless lattice variables we use in simulating the dynamics of the soft color fields. We then explicitly write the discretized equations of motion and initial conditions used in the main body of the paper. In this paper we consider the non-Abelian SU(2) group; however, the equations below are independent of the gauge group considered.

1. Lattice variables

We begin by defining dimensionless lattice variables which will be used in the simulation. We introduce three lattice spacings: a which is the dimensionful transverse spatial lattice spacing, ϵ which is the dimensionful temporal lattice spacing, and a_η which is the dimensionless lattice spacing in the η direction. We rescale space and time

$$\hat{x} = x/a, \quad \hat{y} = y/a, \quad \hat{\eta} = \eta, \quad \hat{\tau} = \tau/a, \quad \hat{\epsilon} = \epsilon/a. \tag{A1}$$

With these definitions we can rescale the field variables, conjugate momenta, and currents and introduce lattice variables with "hats"

$$\hat{A}^i = gaA^i, \quad \hat{A}_\eta = gA_\eta, \quad \hat{\Pi}_i = ga\Pi_i, \quad \hat{\Pi}^\eta = ga^2\Pi^\eta, \tag{A2}$$

and

$$\hat{\bar{W}} = a\bar{W}, \quad \hat{j}^\tau = a^3 j^\tau, \quad \hat{j}^i = a^3 j^i, \quad \hat{j}^\eta = a^4 j^\eta. \tag{A3}$$

Finally, we rescale the isotropic Debye mass via $\hat{m}_D = am_D$. Performing this transformation on the Hamiltonian density we find

$$\mathcal{H} = \frac{\hat{\tau}}{g^2 a^3}\,\mathrm{tr}\left[\frac{1}{\hat{\tau}^2}\hat{F}_{\eta i}^2 + \frac{1}{\hat{\tau}^2}\hat{\Pi}_i^2 + \hat{F}_{xy}^2 + (\hat{\Pi}^\eta)^2\right]. \tag{A4}$$

In the following subsections we will drop the "hats" on symbols. From this point on in this appendix, all variables can be assumed to be dimensionless lattice variables.

2. Plaquettes and staples

We can translate the continuum equations of motion into gauge-invariant lattice equations of motion by using standard plaquette and staple operators. For the transverse coordinate-rapidity plaquettes we have

$$(F_{k\eta})^a = \frac{iN_c}{a_\eta}\,\mathrm{tr}[\tau^a U_{\square,k\eta}], \tag{A5}$$

where $k \in \{x, y\}$, a is a color algebra index, $a \in \{1, \ldots, N_c^2 - 1\}$, and $U_{\square,\mu\nu}(x) = U_\mu(x)U_\nu(x+\mu)\times U_\mu^\dagger(x+\nu)U_\nu^\dagger(x)$ is a standard lattice plaquette variable with U_μ being a parallel transporter in μ direction

$$U_i = \exp(-iA^i), \tag{A6}$$

$$U_\eta = \exp(ia_\eta A_\eta). \tag{A7}$$

Products like $F_{\mu\nu}^2$ which appear in the energy density can also be expressed in terms of plaquette variables.

For this application we need two different combinations, $F^2_{\eta i}$ and F^2_{xy}. These are

$$\mathrm{tr}F^2_{\eta i} = \frac{2}{a_\eta^2}\left(1 - \frac{1}{N_c}\,\mathrm{tr}[\mathrm{Re}U_{\square,\eta i}]\right), \tag{A8}$$

$$\mathrm{tr}F^2_{xy} = 2\left(1 - \frac{1}{N_c}\,\mathrm{tr}[\mathrm{Re}U_{\square,xy}]\right). \tag{A9}$$

Finally, we can rewrite the necessary covariant derivatives acting on the field strength tensor as

$$(D_j F_{jk})^a = iN_c \mathrm{tr}\left[\tau^a U_k(\tau, x) \sum_{|j|\neq k} S^\dagger_{kj}(\tau, x)\right], \tag{A10}$$

$$(D_\eta F_{\eta j})^a = \frac{iN_c}{a_\eta^2}\,\mathrm{tr}\left[\tau^a U_j(\tau, x) \sum_{|\eta|\neq j} S^\dagger_{j\eta}(\tau, x)\right], \tag{A11}$$

$$(D_j F_{j\eta})^a = \frac{iN_c}{a_\eta}\,\mathrm{tr}\left[\tau^a U_\eta(\tau, x) \sum_{|j|\neq \eta} S^\dagger_{\eta j}(\tau, x)\right], \tag{A12}$$

where S is the gauge link staple

$$S^\dagger_{\mu\nu}(\tau, x) = U_\nu(\tau, x+\mu)U^\dagger_\mu(\tau, x+\nu)U^\dagger_\nu(\tau, x). \tag{A13}$$

Note that the sums in (A12) run over both positive and negative directions.

3. Transformation of the $\bar{W}$ fields to a compact domain

In order to better describe $\bar{W}$ in the $\bar{y}$ (shifted rapidity) direction we introduce a velocitylike variable u, $-1 < u < 1$, defined by

$$\bar{y} \equiv \mathrm{atanh}(u), \qquad d\bar{y} = \frac{1}{1-u^2}\,du. \tag{A14}$$

This has the effect of giving more lattice points around $\bar{y} = 0$, where the $\bar{W}$ functions are rapidly varying.

Using $\sinh^2(\bar{y}) = u^2/(1-u^2)$ and $\cosh^2(\bar{y}) = 1/(1-u^2)$ we can rewrite (3.33) as

$$\begin{aligned}\partial_\tau \bar{W}(\tau, \mathbf{x}, \eta; \phi, u) &= -\sqrt{1-u^2}\,v^i D_i \bar{W} - \frac{u}{\tau}(D_\eta \bar{W} - (1-u^2)\partial_u \bar{W}) \\ &\quad + \frac{1}{\bar{f}(\tau, \tau_{\mathrm{iso}}, u)}\left[\frac{1}{\tau}v^i \Pi_i - \frac{\tau^2}{\tau^2_{\mathrm{iso}}}\frac{u}{\sqrt{1-u^2}}\Pi^\eta \right. \\ &\quad \left. + \frac{u}{\tau}\left(1 - \frac{\tau^2}{\tau^2_{\mathrm{iso}}}\right)v^i F_{i\eta}\right],\end{aligned} \tag{A15}$$

where

$$\bar{f}(\tau, \tau_{\mathrm{iso}}, u) = \left(1 + \frac{\tau^2}{\tau^2_{\mathrm{iso}}}\frac{u^2}{1-u^2}\right)^2. \tag{A16}$$

The currents are then given by

$$j^\tau = -\frac{m_D^2}{2}\int_0^{2\pi}\frac{d\phi}{2\pi}\int_{-1}^{1} du(1-u^2)^{-\frac{3}{2}}\bar{W}(\tau, \mathbf{x}, \eta; \phi, u), \tag{A17}$$

$$j^i = -\frac{m_D^2}{2}\int_0^{2\pi}\frac{d\phi}{2\pi}\int_{-1}^{1} du v^i(1-u^2)^{-1}\bar{W}(\tau, \mathbf{x}, \eta; \phi, u), \tag{A18}$$

$$j^\eta = -\frac{m_D^2}{2\tau}\int_0^{2\pi}\frac{d\phi}{2\pi}\int_{-1}^{1} du u(1-u^2)^{-\frac{3}{2}}\bar{W}(\tau, \mathbf{x}, \eta; \phi, u), \tag{A19}$$

where, as usual, $v^i = (\cos\phi, \sin\phi)$ with $i \in \{x, y\}$.

4. Lattice equations of motion

We will express the equations of motion in terms of gauge links U and chromoelectric fields Π. Both U's and Π's live on links (between sites) so all of their spatial arguments have an implicit $+1/2$ shift. In some cases this $1/2$ is made explicit for maximum clarity. Temporally Π's also live between sites. The link variables U, however, temporally live on sites. The $\mathcal{W}$'s and j's live on sites both spatially and temporally. We use a lattice with $N_\perp$ sites in the x and y directions and N_η sites in the η direction. The fields are assumed to be periodic in all directions. We use a leapfrog algorithm in which the conjugate momenta are updated first using fixed links/currents and then the link variables and $\mathcal{W}$ fields are evolved using the updated conjugate momenta [134–138].

The resulting Yang-Mills update equations are

$$\Pi_i\left(\tau + \frac{\epsilon}{2}, \mathbf{x}, \eta\right) = \Pi_i\left(\tau - \frac{\epsilon}{2}, \mathbf{x}, \eta\right) + \tau\epsilon\left(j^i_{\mathrm{avg}}(\tau, \mathbf{x}, \eta) + D_j F_{ji}(\tau, \mathbf{x}, \eta) + \frac{1}{\tau^2}D_\eta F_{\eta i}(\tau, \mathbf{x}, \eta)\right), \tag{A20}$$

$$\Pi^\eta\left(\tau + \frac{\epsilon}{2}, \mathbf{x}, \eta\right) = \Pi^\eta\left(\tau - \frac{\epsilon}{2}, \mathbf{x}, \eta\right) - \frac{\epsilon}{\tau}(\tau^2 j^\eta_{\mathrm{avg}}(\tau, \mathbf{x}, \eta) + D_i F_{i\eta}(\tau, \mathbf{x}, \eta)), \tag{A21}$$

$$U_i(\tau+\epsilon,\mathbf{x},\eta)=\exp\left(-i\epsilon\tau^{-1}\Pi_i\left(\tau+\frac{\epsilon}{2},\mathbf{x},\eta\right)\right)U_i(\tau,\mathbf{x},\eta), \tag{A22}$$

$$U_\eta(\tau+\epsilon,\mathbf{x},\eta)=\exp\left(+i\epsilon\tau a_\eta\Pi^\eta\left(\tau+\frac{\epsilon}{2},\mathbf{x},\eta\right)\right)U_\eta(\tau,\mathbf{x},\eta), \tag{A23}$$

where

$$j^i_{\rm avg}(\tau,\mathbf{x},\eta)\equiv\frac{1}{2}[j^i(\tau,\mathbf{x},\eta)+U_i^\dagger(\tau,\mathbf{x},\eta)j^i(\tau,\mathbf{x}+\hat{\mathbf{e}}_i,\eta)U_i(\tau,\mathbf{x},\eta)], \tag{A24}$$

$$j^\eta_{\rm avg}(\tau,\mathbf{x},\eta)\equiv\frac{1}{2}[j^\eta(\tau,\mathbf{x},\eta)+U_\eta^\dagger(\tau,\mathbf{x},\eta)j^\eta(\tau,\mathbf{x},\eta+1)U_\eta(\tau,\mathbf{x},\eta)]. \tag{A25}$$

To discretize the $\bar{W}$ fields we use a rectangular lattice in ϕ-u space of size $N_\phi\times N_u$ and

$$\phi_n=2\pi n/N_\phi, \tag{A26}$$

$$u_m=-1+(2m+1)/N_u, \tag{A27}$$

where $n\in\{0,\cdots,N_\phi-1\}$ and $m\in\{0,\cdots,N_u-1\}$.

The update equations for the $\bar{W}$ fields then take the form

$$\begin{aligned}\bar{W}(\tau+\epsilon,\mathbf{x},\eta;\phi,u)&=\bar{W}(\tau-\epsilon,\mathbf{x},\eta;\phi,u)+2\epsilon\Bigg\{-\sqrt{1-u^2}v^iD_i^S\bar{W}\\&-\frac{u}{\tau}(D_\eta^S\bar{W}-(1-u^2)\partial_u^S\bar{W})+\frac{1}{\bar{f}(\tau,\tau_{\rm iso},u)}\\&\times\left[\frac{1}{\tau}v^i\Pi_i^{\rm avg}-\frac{\tau^2}{\tau_{\rm iso}^2}\frac{u}{\sqrt{1-u^2}}\Pi^\eta_{\rm avg}+\frac{u}{\tau}\left(1-\frac{\tau^2}{\tau_{\rm iso}^2}\right)v^iF_{i\eta}\right]\Bigg\},\end{aligned} \tag{A28}$$

where $F_{i\eta}$ is computed using plaquettes via Eq. (A5), D_i^S and D_η^S are symmetric covariant derivatives in the transverse and rapidity directions, respectively,

$$\begin{aligned}D_\eta^S\varphi(\eta)\equiv&\frac{1}{2a_\eta}(U_\eta^\dagger(\eta)\varphi(\eta+1)U_\eta(\eta)\\&-U_\eta(\eta-1)\varphi(\eta-1)U_\eta^\dagger(\eta-1)),\end{aligned} \tag{A29}$$

$$\begin{aligned}D_i^S\varphi(x_i)\equiv&\frac{1}{2}(U_i^\dagger(x_i)\varphi(x_i+1)U_i(x_i)\\&-U_i(x_i-1)\varphi(x_i-1)U_i^\dagger(x_i-1)),\end{aligned} \tag{A30}$$

and ∂_u^S is a symmetric derivative in u space

$$\partial^S\varphi(u_m)\equiv\frac{\varphi(u_{m+1})-\varphi(u_{m-1})}{2\Delta u}, \tag{A31}$$

where $\Delta u=2/N_u$. The averaged conjugate momenta, $\Pi_i^{\rm avg}$ and $\Pi^\eta_{\rm avg}$, appearing in (A28) are averaged both spatially and temporally

$$\Pi_i^{\rm avg}(\tau,\mathbf{x},\eta)=\frac{1}{16}\sum_{\sigma_x=\pm1}\sum_{\sigma_y=\pm1}\sum_{\sigma_\eta=\pm1}\sum_{\sigma_\tau=\pm1}\mathcal{P}_{\mathcal{T}}\Pi_i\left(\tau+\frac{\sigma_\tau}{2},x+\frac{\sigma_x}{2},y+\frac{\sigma_y}{2},\eta+\frac{\sigma_\eta}{2}\right), \tag{A32}$$

$$\Pi^\eta_{\rm avg}(\tau,\mathbf{x},\eta)=\frac{1}{16}\sum_{\sigma_x=\pm1}\sum_{\sigma_y=\pm1}\sum_{\sigma_\eta=\pm1}\sum_{\sigma_\tau=\pm1}\mathcal{P}_{\mathcal{T}}\Pi^\eta\left(\tau+\frac{\sigma_\tau}{2},x+\frac{\sigma_x}{2},y+\frac{\sigma_y}{2},\eta+\frac{\sigma_\eta}{2}\right), \tag{A33}$$

where we have indicated explicitly the fact that the Π's live on links (halfway between sites) for clarity and $\mathcal{P}_{\mathcal{T}}$ stands for the parallel transporter necessary to bring the conjugate momenta to the same site.

The currents are computed from the $\bar{W}$ fields via

$$j^\tau(\tau,\mathbf{x},\eta)=-\frac{m_D^2}{N_\phi N_u}\sum_{n,m}(1-u^2)^{-\frac{3}{2}}\bar{W}(\tau,\mathbf{x},\eta;\phi,u), \tag{A34}$$

$$j^i(\tau,\mathbf{x},\eta)=-\frac{m_D^2}{N_\phi N_u}\sum_{n,m}v^i(1-u^2)^{-1}\bar{W}(\tau,\mathbf{x},\eta;\phi,u), \tag{A35}$$

$$j^\eta(\tau,\mathbf{x},\eta)=-\frac{m_D^2}{\tau N_\phi N_u}\sum_{n,m}u(1-u^2)^{-\frac{3}{2}}\bar{W}(\tau,\mathbf{x},\eta;\phi,u), \tag{A36}$$

and we monitor Gauss's law by periodically checking

$$\mathrm{tr}\Big[\frac{1}{N_\perp^2 N_\eta}\sum_{\mathbf{x},\eta}\tau j^\tau(\tau,\mathbf{x},\eta)+D_\eta^S\Pi^\eta_{\mathrm{avg}}(\tau,\mathbf{x},\eta) - D_i^S\Pi_i^{\mathrm{avg}}(\tau,\mathbf{x},\eta)\Big]^2. \quad \text{(A37)}$$

We compute the discretized transverse and longitudinal contributions to the field energy density $\mathcal{E}$ via

$$\mathcal{E}_T=\frac{1}{N_\perp^2 N_\eta}\sum_{\mathbf{x},\eta}\mathrm{tr}[\tau^{-2}F_{\eta i}^2+\tau^{-2}\Pi_i^2], \quad \text{(A38)}$$

$$\mathcal{E}_L=\frac{1}{N_\perp^2 N_\eta}\sum_{\mathbf{x},\eta}\mathrm{tr}[F_{xy}^2+(\Pi^\eta)^2], \quad \text{(A39)}$$

where $\mathrm{tr}F_{\eta i}^2$ and $\mathrm{tr}F_{xy}^2$ are computed using Eqs. (A8) and (A9).

APPENDIX B: CHOICE OF LATTICE PARAMETERS

In this appendix we detail the constraints which should be obeyed in order for our simulations to properly describe the soft gauge field dynamics. Since the soft scale is time dependent, we have to choose parameters which allow for a faithful representation of the infrared and ultraviolet physics during the entirety of the simulation.

The physical (dimensionful) parameter m_D^2 is the Debye mass at time τ_{iso}. In terms of the gluon liberation factor c which is $\mathcal{O}(1)$ ($\simeq 1.1$ according to Lappi [94], $c=2\ln 2\approx 1.386$ according to Kovchegov [91]) one has

$$m_D^2\tau_{\mathrm{iso}}\tau_0\approx 0.93c(Q_s\tau_0). \quad \text{(B1)}$$

In the text we use $Q_s\tau_0=1$ and $c=2\ln 2$ from Kovchegov [91]. This gives $m_D^2\tau_{\mathrm{iso}}\tau_0=1.285$. For large anisotropy one finds

$$m_\infty^2(\tau)\simeq\frac{\pi}{4}m_D^2\tau_{\mathrm{iso}}/\tau, \quad \text{(B2)}$$

which can be taken as the typical (time-dependent) soft momentum scale. With our choice of $c=2\ln 2$, we have $m_\infty(\tau)\approx 1.0(\tau_0\tau)^{-1/2}$. For RHIC energies one has $\tau_0^{-1}=Q_s\sim 1.4$ GeV and at current LHC energies one has $Q_s\sim 2$ GeV. At RHIC and LHC energies $\tau_0=Q_s^{-1}$ correspond to 0.14 fm/c and 0.1 fm/c, respectively.

On a lattice with periodic boundary conditions, the size of the lattice determines the infrared cutoff in full wavelengths and the lattice spacing determines the ultraviolet cutoff via the smallest half wavelength. In our expanding system, the transverse UV cutoff is constant in time and given by π/a, whereas the soft momentum scale is decreasing in time. It is therefore sufficient to ensure

$$k_{\max}=\frac{\pi}{a}\gg m_\infty(\tau_0), \quad \text{(B3)}$$

so that we should demand $a\lesssim 1\tau_0$.

In longitudinal direction, the effective UV cutoff is decreasing in time according to $\pi/(\tau a_\eta)$. We may choose for example

$$\frac{\tau_{\max}}{2}a_\eta\sim a, \quad \text{(B4)}$$

to have comparable transverse and longitudinal UV cutoffs in an average sense. More importantly, the maximal longitudinal wave number of unstable modes increases in time, so $\nu_{\max}$ should be a large number,

$$\nu_{\max}=\frac{\pi}{a_\eta}\gg 30. \quad \text{(B5)}$$

Since the hard-expanding-loop framework is designed to treat the soft sector of the dynamics, it is somewhat more important to properly treat the infrared scale. In the longitudinal direction $\nu_{\min}=2\pi/(N_\eta a_\eta)$ should be made as low as possible. There are no important unstable modes with ν much smaller than 5, but $\nu_{\min}$ also sets the spacing between mode numbers. We should therefore aim at

$$\nu_{\min}=\frac{2\pi}{N_\eta a_\eta}\ll 5. \quad \text{(B6)}$$

In the transverse direction, the semianalytic results [84,86] suggest that we should have

$$k_{\min}=\frac{2\pi}{N_\perp a}\ll 0.2\tau_0^{-1}. \quad \text{(B7)}$$

As our canonical set of parameters in the results section we use $N_T=40$, $N_\eta=128$, $a_\eta=0.025$, $a=Q_s^{-1}$, and $\tau_0=Q_s^{-1}$. Checking the transverse infrared cutoff one finds $k_{\min}=0.157Q_s<0.2Q_s$ as required. Checking the transverse ultraviolet cutoff one finds $k_{\max}=\pi Q_s>1.005Q_s$ as required. Checking the longitudinal infrared cutoff one finds $\nu_{\min}=1.96<5$ as required. Finally, checking the longitudinal ultraviolet cutoff one finds $\nu_{\max}=125.7>30$.

APPENDIX C: INITIAL CONDITIONS

In this appendix we collect details of the initial conditions used in the simulations and some information about lattice initial conditions in general.

1. Gaussian random variables

We now discuss the scalings necessary when sampling lattice variables from Gaussian distributions. For completeness we list all possible types of initial conditions; however, in the body of the text we use exclusively initial conditions based on current fluctuations. We then give some more details about the precise implementation of the current fluctuation initial conditions used in the body of the text.

It is common to use uncorrelated Gaussian random noise as the initial condition for either fields or current fluctuations. In the case of uncorrelated transverse vector potentials, for example, one assumes that in the continuum limit

$$\langle A_i^a(\tau_0,\mathbf{x}_1,\eta_1)A_j^b(\tau_0,\mathbf{x}_2,\eta_2)\rangle = \Delta^2\delta^{ab}\delta_{ij}\delta^{(2)}(\mathbf{x}_1-\mathbf{x}_2)\delta(\eta_1-\eta_2), \quad \text{(C1)}$$

where $\mathbf{x}^\perp \equiv (x, y)$ is a purely transverse two-vector. In order to translate this statement into something useful for the lattice initial conditions we should convert to dimensionless variables on the left- and right-hand sides. In doing so we make use of the rescalings specified in Eqs. (A1) and (A2) and the Dirac delta function identity $\delta(ax) = \delta(x)/|a|$ to obtain [in terms of the lattice variables introduced in Eqs. (A2) and (A3)]

$$\langle A_i^a(\tau_0, \mathbf{x}_1^\perp, \eta_1) A_j^b(\tau_0, \mathbf{x}_2^\perp, \eta_2)\rangle = \frac{g^2\Delta^2}{a_\eta}\delta^{ab}\delta_{ij}\delta_{x_1^\perp x_2^\perp}\delta_{\eta_1\eta_2}. \tag{C2}$$

In practice, this means that the A_i variables should be Gaussian random numbers with a standard deviation of $\sigma = g\Delta/a_\eta^{1/2}$.

Using similar arguments we can derive the following lattice correlation functions in the case that we initialize longitudinal vector potentials:

$$\langle A_\eta^a(\tau_0, \mathbf{x}_1^\perp, \eta_1) A_\eta^b(\tau_0, \mathbf{x}_2^\perp, \eta_2)\rangle = \frac{g^2\Delta^2}{a^2 a_\eta}\delta^{ab}\delta_{x_1^\perp x_2^\perp}\delta_{\eta_1\eta_2}, \tag{C3}$$

or transverse momenta

$$\langle \Pi_i^a(\tau_0, \mathbf{x}_1^\perp, \eta_1)\Pi_j^b(\tau_0, \mathbf{x}_2^\perp, \eta_2)\rangle = \frac{g^2\Delta^2}{a_\eta}\delta^{ab}\delta_{ij}\delta_{x_1^\perp x_2^\perp}\delta_{\eta_1\eta_2}, \tag{C4}$$

or longitudinal momenta

$$\langle \Pi_\eta^a(\tau_0, \mathbf{x}_1^\perp, \eta_1)\Pi_\eta^b(\tau_0, \mathbf{x}_2^\perp, \eta_2)\rangle = \frac{g^2 a^2\Delta^2}{a_\eta}\delta^{ab}\delta_{x_1 x_2}\delta_{\eta_1\eta_2}, \tag{C5}$$

or auxiliary fields

$$\langle W^{a\alpha}(\tau_0, \mathbf{x}_1^\perp, \eta_1; \phi_1, y_1) W^{b\beta}(\tau_0, \mathbf{x}_2^\perp, \eta_2; \phi_2, y_2)\rangle = \frac{\Delta^2}{a_\eta}\delta^{ab}\delta^{\alpha\beta}\delta_{x_1^\perp x_2^\perp}\delta_{y_1 y_2}\delta_{\eta_1\eta_2}\delta_{\phi_1\phi_2}. \tag{C6}$$

To summarize, when using Gaussian random initial conditions on anisotropic lattices, one should choose the standard deviations shown in Table I. Moreover, unless initial fluctuations are only set up for the gauge fields A_i^a and A_η^a, a projection to satisfy the Gauss law constraint (3.26) is needed. In our simulations we have however used a different setup which we now discuss.

TABLE I. Transverse and longitudinal lattice spacing scaling for a variety of different initial condition types.

Case	Std. Dev. (σ)
Transverse Vector Potential (A_i)	$g\Delta/a_\eta^{1/2}$
Longitudinal Vector Potential (A_η)	$g\Delta/(aa_\eta^{1/2})$
Transverse Conjugate Momentum (Π_i)	$g\Delta/a_\eta^{1/2}$
Longitudinal Conjugate Momentum (Π_η)	$ga\Delta/a_\eta^{1/2}$
Current fluctuations ($\mathcal{W}$)	$\Delta/a_\eta^{1/2}$

2. Initial condition setup

The analytic study of collective modes in anisotropically expanding ultrarelativistic plasmas [86] has found that the initial fluctuations in (only) induced currents versus only initial fluctuations in collective fields reduces considerably the delay of the onset of the plasma instabilities. As discussed in Sec. IV, this means that such initial conditions dominate over all other possibilities, and it is therefore sufficient to concentrate on initial fluctuations in the W fields which directly encode the induced currents.

a. Longitudinal current initial conditions

For oblate anisotropy, fluctuations in longitudinal currents give rise to stable plasmon modes, and in the Abelian case they do not lead to any plasma instabilities. We have used this to test our code for unphysical instabilities (see Appendix D).

The simplest initial fluctuations consistent with Gauss's law which achieve this are fluctuations in only the $W^{a\eta}$ components that are independent of ϕ and y (thereby ensuring that initially $j^\tau = 0$) but nothing else

$$\langle W^{a\eta}(\tau_0, \mathbf{x}_1^\perp, \eta_1; \phi_1, y_1) W^{b\eta}(\tau_0, \mathbf{x}_2^\perp, \eta_2; \phi_2, y_2)\rangle = \frac{\Delta^2}{a_\eta}\delta^{ab}\delta_{x_1^\perp x_2^\perp}\delta_{\eta_1\eta_2},$$
$$W^{ai} = 0, \quad U_{s+\frac{1}{2}} = \mathbf{1}_{N_c}, \quad \Pi_{i,s} = \Pi_{\eta,s} = 0. \tag{C7}$$

b. Transversal current initial conditions

In order to provide seed fields for Weibel instabilities, longitudinal current fluctuations do not play an important role (for oblate anisotropies). For simplicity we have therefore only considered transverse current fluctuations by only initializing W^{ai} fields. Because we have used rather fine lattices in the η direction, Gaussian random noise would correspond to very high UV noise in longitudinal wave numbers even beyond the scale which separates soft and hard modes, while hard modes are already integrated out. We have therefore introduced a mode number cutoff Λ_ν such that $\nu_{\max} = \Lambda_\nu \nu_{\min}$ with $\nu_{\min} = 2\pi/(N_\eta a_\eta)$. Again, the simplest initial fluctuations consistent with the Gauss law are obtained by requiring that the W^{ai} components are independent of ϕ and y, and thus initially $j^\tau = 0$, while setting all other fields to zero initially. This is now done in terms of the Fourier components $\tilde{W}^{ai}$ with $W^{ai}(\ldots, \eta, \ldots) = \sum_\nu \tilde{W}^{ai}(\ldots, \nu, \ldots)e^{i\nu\eta}$ according to

$$\langle \tilde{W}^{ai}(\tau_0, \mathbf{x}_1^\perp, \nu_1; \phi_1, y_1)\tilde{W}^{bj}(\tau_0, \mathbf{x}_2^\perp, \nu_2; \phi_2, y_2)\rangle = \Delta^2\delta^{ab}\delta^{ij}\delta_{x_1^\perp x_2^\perp}\delta_{\nu_1,-\nu_2}\theta(\nu_{\max} - |\nu_1|),$$
$$W^{a\eta} = 0, \quad U_{s+\frac{1}{2}} = \mathbf{1}_{N_c}, \quad \Pi_{i,s} = \Pi_{\eta,s} = 0. \tag{C8}$$

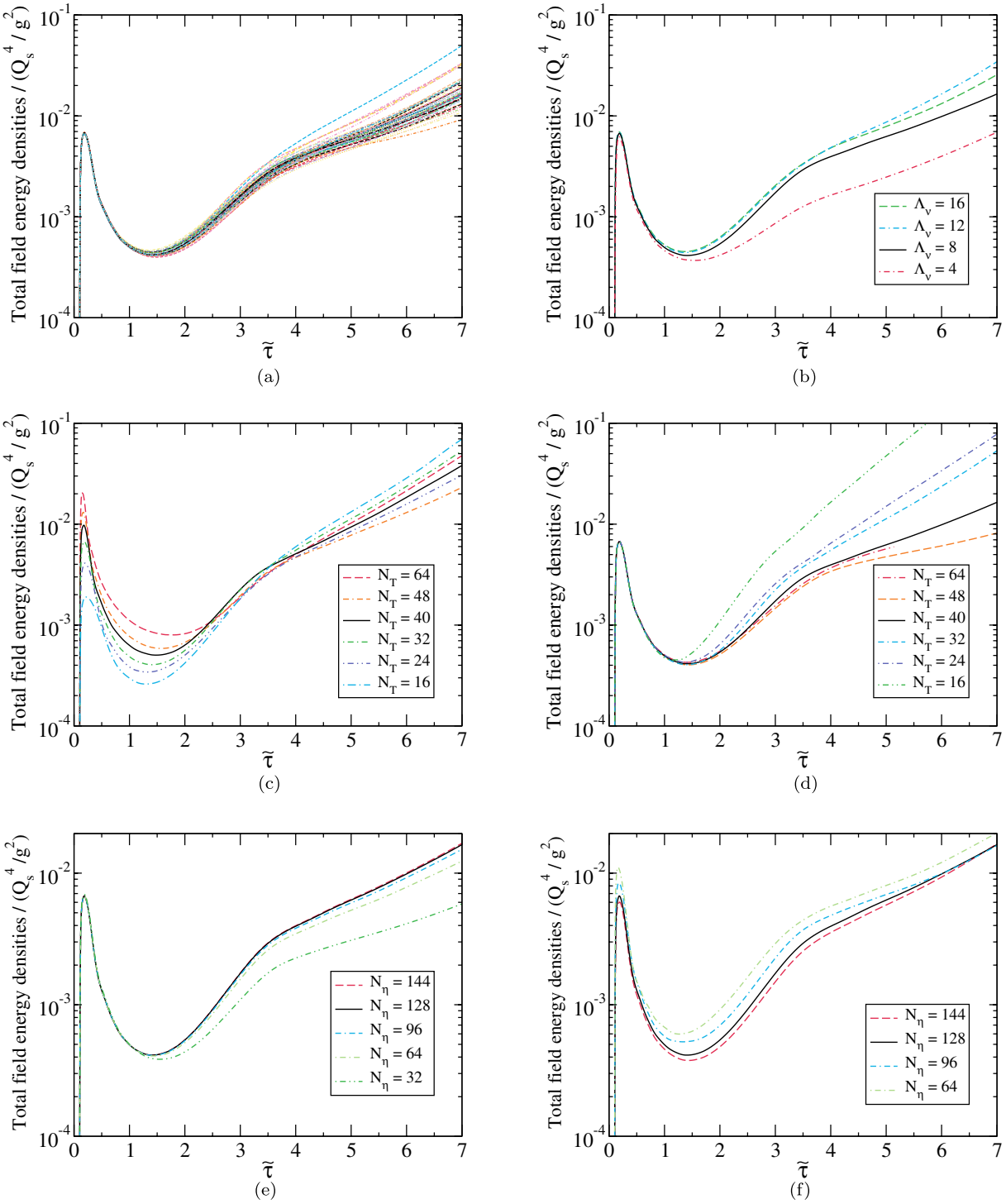

FIG. 12 (color online). Collected numerical tests of unstable mode growth. Each subpanel shows the chromofield total energy density evolution subject to variation of various parameters. The subcaptions contain a description of the parameters which are varied. (a) Variation of the initial random seed used for the current fluctuations (50 different runs). All parameters are the same as in Fig. 3, (b) Variation of the longitudinal cutoff, $\Lambda_\nu\,\nu_{\min}$ with $\nu_{\min} = 1.96$, for the current fluctuation initial conditions. All parameters except Λ_ν are the same as in Fig. 3, (c) Variation of the transverse lattice spacing, a, while keeping the transverse lattice size, $L_T = N_T\,a$, fixed. All parameters except a and N_T are the same as in Fig. 3, (d) Variation of the transverse lattice size, $L_T = N_T\,a$, while keeping the transverse lattice spacing, a, fixed. All parameters except N_T are the same as in Fig. 3, (e) Variation of the longitudinal lattice spacing, a_η, while keeping the longitudinal lattice size, $L_\eta = N_\eta a_\eta$, fixed. All parameters except a_η and N_η are the same as in Fig. 3, and (f) Variation of the longitudinal lattice size, $L_\eta = N_\eta a_\eta$, while keeping the longitudinal lattice spacing, a_η, fixed. All parameters except N_η and Δ are the same as in Fig. 3.

APPENDIX D: NUMERICAL TESTS

In this section we collect various numerical tests such as varying the lattice spacing, lattice size, spectral cutoffs, and velocity-space resolution. In Fig. 12 we collect six different tests. The variation with the random seed used for generating the necessary pseudorandom numbers used in the initial conditions is shown in Fig. 12(a). As we can see from this figure there is a fair amount of variation with the random seed used; however, the results are all qualitatively the same. In the results section our main results are averaged over the set of runs shown in Fig. 12(a).

The variation with the ultraviolet longitudinal mode cutoff used for initializing the initial current fluctuations via the auxiliary $\mathcal{W}$ fields is shown in Fig. 12(b). As can be seen from this figure there is a rapid convergence as the ultraviolet cutoff $\Lambda_\nu \nu_{\min}$ is increased. The set of runs shown in the main body of the text uses $\Lambda_\nu = 8$.

The variation with the transverse lattice spacing while holding the transverse lattice size fixed is shown in Fig. 12(c). This represents a test of the approach to the continuum as the transverse lattice resolution is increased. In the transverse plane we sample Gaussian random numbers which means as the lattice spacing decreases the transverse configurations will be dominated by the high transverse momentum part of the fluctuations. This is evidenced by the fact that the initial energy density deposited in the fields by the current fluctuations increases rapidly as one approaches the transverse continuum limit. One could remove this artifact by implementing a transverse mode cutoff on the lattice, but at this point in time we have not yet done so. In the results section our standard set of runs uses $N_T = 40$.

The variation with the transverse lattice size while holding the transverse lattice spacing fixed is shown in Fig. 12(d). In this case we see a rather large effect. In the limit that $N_T \to 1$ while holding a fixed, one approaches a one-dimensional system which exhibits a faster growth rate due to less mode competition. We have verified that in this limit we reproduce our previously obtained results from Ref. [85]. The faster growth seen compared to Ref. [85] is due to the use of the more general initial conditions which include current fluctuations [86]. In the results section our standard set of runs uses $N_T = 40$.

The variation with the longitudinal lattice spacing while holding the longitudinal lattice size fixed is shown in Fig. 12(e). Due to the fact that we have implemented an ultraviolet cutoff on fluctuations in the η direction, we see a very nice convergence as the lattice resolution in the η direction is increased. In the results section our standard set of runs uses $N_T = 40$. In the results section our standard set of runs uses $N_\eta = 128$.

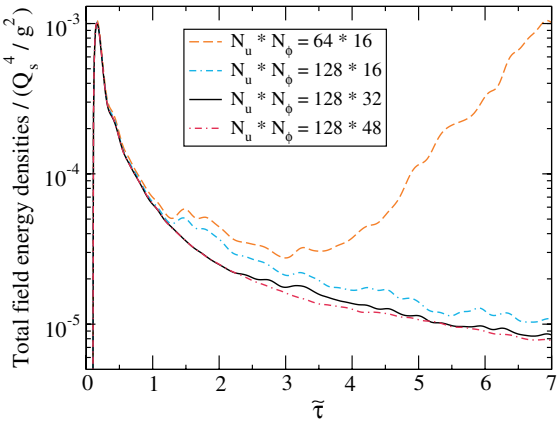

FIG. 13 (color online). Evolution of a stable configuration initialized with Abelian longitudinal currents for different sized velocity lattices.

The variation with the longitudinal lattice size while holding the longitudinal lattice spacing fixed is shown in Fig. 12(f). (Here Δ has been adjusted to correct for the different initial spectrum which starts at smaller $\nu_{\min}$ with larger N_η, leading to different initial energy densities.) Once again we see only small variation with the assumed longitudinal lattice size, with the late-time variations being consistent with those coming from random seed variation. In the results section our standard set of runs uses $N_\eta = 128$.

Finally, in Fig. 13 we show the evolution of a stable Abelian configuration initialized with Abelian longitudinal currents for various different velocity lattice resolutions $N_u \times N_\phi \in \{64 \times 16, 128 \times 16, 128 \times 32, 128 \times 48\}$. For this simulation the lattice spatial size was $N_T^2 \times N_\eta = 32^2 \times 32$ with transverse lattice spacing of $a = 0.1$ fm and longitudinal lattice spacing of $a_\eta = 0.025$. The initial time was taken to be $\tau_0 = 0.1$ fm/c and we used $\tau_{\text{iso}} = 0.01$ fm/c. For the temporal time step we use $\epsilon = 10^{-3}$ fm/c. With these initial conditions, the field energy should decay steadily after the initial peak. This test turns out to be very sensitive to the velocity-space resolution, i.e., the number of $\mathcal{W}$ fields. If this resolution is too crude, the field energy even grows at late times. Figure 13 shows that with a velocity lattice size of $N_u \times N_\phi = 128 \times 32$ there is already good convergence to the correct time evolution of the system. Unstable modes are in fact less sensitive to the velocity resolution in the ϕ direction; however, being cautious we have performed all simulations using $N_u \times N_\phi = 128 \times 32$.

[1] P. Huovinen, P. F. Kolb, U. W. Heinz, P. V. Ruuskanen, and S. A. Voloshin, Phys. Lett. B **503**, 58 (2001).
[2] T. Hirano and K. Tsuda, Phys. Rev. C **66**, 054905 (2002).
[3] M. J. Tannenbaum, Rep. Prog. Phys. **69**, 2005 (2006).
[4] P. F. Kolb and U. W. Heinz, in *Quark Gluon Plasma*, edited by R. C. Hwa *et al.* (World Scientific, Singapore, 2003), pp. 634–714.
[5] A. Muronga, Phys. Rev. Lett. **88**, 062302 (2002).
[6] A. Muronga, Phys. Rev. C **69**, 034903 (2004).
[7] A. Muronga and D. H. Rischke, arXiv:nucl-th/0407114.
[8] R. Baier, P. Romatschke, and U. A. Wiedemann, Phys. Rev. C **73**, 064903 (2006).
[9] P. Romatschke and U. Romatschke, Phys. Rev. Lett. **99**, 172301 (2007).
[10] R. Baier, P. Romatschke, D. T. Son, A. O. Starinets, and M. A. Stephanov, J. High Energy Phys. 04 (2008) 100.
[11] K. Dusling and D. Teaney, Phys. Rev. C **77**, 034905 (2008).
[12] M. Luzum and P. Romatschke, Phys. Rev. C **78**, 034915 (2008).
[13] H. Song and U. W. Heinz, J. Phys. G **36**, 064033 (2009).
[14] U. W. Heinz, *Relativistic Heavy Ion Physics*, edited by R. Stock, Landolt-Boernstein New Series, Vol. I/23 (Springer-Verlag, New York, 2010), Chap. 5.
[15] A. El, Z. Xu, and C. Greiner, Phys. Rev. C **81**, 041901 (2010).
[16] J. Peralta-Ramos and E. Calzetta, Phys. Rev. D **80**, 126002 (2009).
[17] J. Peralta-Ramos and E. Calzetta, Phys. Rev. C **82**, 054905 (2010).
[18] G. Denicol, T. Kodama, and T. Koide, J. Phys. G **37**, 094040 (2010).
[19] G. Denicol, T. Koide, and D. Rischke, Phys. Rev. Lett. **105**, 162501 (2010).
[20] B. Schenke, S. Jeon, and C. Gale, Phys. Rev. Lett. **106**, 042301 (2011).
[21] B. Schenke, S. Jeon, and C. Gale, Phys. Lett. B **702**, 59 (2011).
[22] C. Shen, U. Heinz, P. Huovinen, and H. Song, Phys. Rev. C **84**, 044903 (2011).
[23] P. Bozek, Phys. Lett. B **699**, 283 (2011).
[24] H. Niemi, G. S. Denicol, P. Huovinen, E. Molnar, and D. H. Rischke, Phys. Rev. Lett. **106**, 212302 (2011).
[25] H. Niemi, G. Denicol, P. Huovinen, E. Molnar, and D. Rischke, Phys. Rev. C **86**, 014909 (2012).
[26] P. Bozek and I. Wyskiel-Piekarska, Phys. Rev. C **85**, 064915 (2012).
[27] G. Denicol, H. Niemi, E. Molnar, and D. Rischke, Phys. Rev. D **85**, 114047 (2012).
[28] R. Ryblewski and W. Florkowski, Phys. Rev. C **85**, 064901 (2012).
[29] M. P. Heller, R. A. Janik, and P. Witaszczyk, Phys. Rev. Lett. **108**, 201602 (2012).
[30] M. P. Heller, R. A. Janik, and P. Witaszczyk, Phys. Rev. D **85**, 126002 (2012).
[31] B. Wu and P. Romatschke, Int. J. Mod. Phys. C **22**, 1317 (2011).
[32] M. Martinez and M. Strickland, Phys. Rev. C **79**, 044903 (2009).
[33] W. Florkowski and R. Ryblewski, Phys. Rev. C **83**, 034907 (2011).
[34] M. Martinez and M. Strickland, Nucl. Phys. **A848**, 183 (2010).
[35] R. Ryblewski and W. Florkowski, J. Phys. G **38**, 015104 (2011).
[36] M. Martinez and M. Strickland, Nucl. Phys. **A856**, 68 (2011).
[37] R. Ryblewski and W. Florkowski, Eur. Phys. J. C **71**, 1761 (2011).
[38] W. Florkowski and R. Ryblewski, Phys. Rev. C **85**, 044902 (2012).
[39] M. Martinez, R. Ryblewski, and M. Strickland, Phys. Rev. C **85**, 064913 (2012).
[40] U. W. Heinz, Nucl. Phys. **A418**, 603 (1984).
[41] S. Mrowczynski, Phys. Lett. B **214**, 587 (1988).
[42] Y. Pokrovsky and A. Selikhov, JETP Lett. **47**, 12 (1988).
[43] S. Mrowczynski, Phys. Lett. B **314**, 118 (1993).
[44] S. Mrowczynski and M. H. Thoma, Phys. Rev. D **62**, 036011 (2000).
[45] J. Randrup and S. Mrowczynski, Phys. Rev. C **68**, 034909 (2003).
[46] P. Romatschke and M. Strickland, Phys. Rev. D **68**, 036004 (2003).
[47] P. B. Arnold, J. Lenaghan, and G. D. Moore, J. High Energy Phys. 08 (2003) 002.
[48] P. B. Arnold and J. Lenaghan, Phys. Rev. D **70**, 114007 (2004).
[49] P. Romatschke and M. Strickland, Phys. Rev. D **70**, 116006 (2004).
[50] P. B. Arnold, J. Lenaghan, G. D. Moore, and L. G. Yaffe, Phys. Rev. Lett. **94**, 072302 (2005).
[51] E. S. Weibel, Phys. Rev. Lett. **2**, 83 (1959).
[52] S. Mrowczynski, A. Rebhan, and M. Strickland, Phys. Rev. D **70**, 025004 (2004).
[53] A. Rebhan, P. Romatschke, and M. Strickland, Phys. Rev. Lett. **94**, 102303 (2005).
[54] A. Rebhan, P. Romatschke, and M. Strickland, J. High Energy Phys. 09 (2005) 041.
[55] A. Ipp, A. Rebhan, and M. Strickland, Phys. Rev. D **84**, 056003 (2011).
[56] P. B. Arnold, G. D. Moore, and L. G. Yaffe, Phys. Rev. D **72**, 054003 (2005).
[57] P. B. Arnold and G. D. Moore, Phys. Rev. D **73**, 025013 (2006).
[58] P. B. Arnold and G. D. Moore, Phys. Rev. D **73**, 025006 (2006).
[59] D. Bodeker and K. Rummukainen, J. High Energy Phys. 07 (2007) 022.
[60] P. B. Arnold and G. D. Moore, Phys. Rev. D **76**, 045009 (2007).
[61] M. Strickland, J. Phys. G **34**, S429 (2007).
[62] J. Berges, S. Scheffler, and D. Sexty, Phys. Rev. D **77**, 034504 (2008).
[63] J. Berges, S. Scheffler, and D. Sexty, Phys. Lett. B **681**, 362 (2009).
[64] J. Berges, D. Gelfand, S. Scheffler, and D. Sexty, Phys. Lett. B **677**, 210 (2009).
[65] J. Berges, J. Pruschke, and A. Rothkopf, Phys. Rev. D **80**, 023522 (2009).
[66] J. Berges, K. Boguslavski, and S. Schlichting, Phys. Rev. D **85**, 076005 (2012).
[67] A. Czajka and S. Mrowczynski, Phys. Rev. D **83**, 045001 (2011).

[68] A. Czajka and S. Mrowczynski, Phys. Rev. D **86**, 025017 (2012).
[69] A. Dumitru and Y. Nara, Phys. Lett. B **621**, 89 (2005).
[70] A. Dumitru, Y. Nara, and M. Strickland, Phys. Rev. D **75**, 025016 (2007).
[71] A. Dumitru, Y. Nara, B. Schenke, and M. Strickland, Phys. Rev. C **78**, 024909 (2008).
[72] D. Bodeker, J. High Energy Phys. 10 (2005) 092.
[73] S. Mrowczynski, Proc. Sci. CPOD2006 (2006) 042 [arXiv:hep-ph/0611067].
[74] S. Mrowczynski and B. Muller, Phys. Rev. D **81**, 065021 (2010).
[75] M. Carrington and A. Rebhan, Eur. Phys. J. C **71**, 1787 (2011).
[76] A. Kurkela and G. D. Moore, J. High Energy Phys. 12 (2011) 044.
[77] A. Kurkela and G. D. Moore, J. High Energy Phys. 11 (2011) 120.
[78] P. Romatschke and R. Venugopalan, Phys. Rev. Lett. **96**, 062302 (2006).
[79] P. Romatschke and R. Venugopalan, Phys. Rev. D **74**, 045011 (2006).
[80] K. Fukushima, F. Gelis, and L. McLerran, Nucl. Phys. **A786**, 107 (2007).
[81] K. Dusling, F. Gelis, and R. Venugopalan, Nucl. Phys. **A872**, 161 (2011).
[82] K. Fukushima and F. Gelis, Nucl. Phys. **A874**, 108 (2012).
[83] K. Dusling, T. Epelbaum, F. Gelis, and R. Venugopalan, Phys. Rev. D **86**, 085040 (2012).
[84] P. Romatschke and A. Rebhan, Phys. Rev. Lett. **97**, 252301 (2006).
[85] A. Rebhan, M. Strickland, and M. Attems, Phys. Rev. D **78**, 045023 (2008).
[86] A. Rebhan and D. Steineder, Phys. Rev. D **81**, 085044 (2010).
[87] T. Lappi and L. McLerran, Nucl. Phys. **A772**, 200 (2006).
[88] G. Baym, Phys. Lett. **138B**, 18 (1984).
[89] A. H. Mueller, Phys. Lett. B **475**, 220 (2000).
[90] R. Baier, A. H. Mueller, D. Schiff, and D. Son, Phys. Lett. B **539**, 46 (2002).
[91] Y. V. Kovchegov, Nucl. Phys. **A692**, 557 (2001).
[92] A. Krasnitz and R. Venugopalan, Nucl. Phys. **A698**, 209 (2002).
[93] A. Krasnitz, Y. Nara, and R. Venugopalan, Nucl. Phys. **A727**, 427 (2003).
[94] T. Lappi, Eur. Phys. J. C **55**, 285 (2008).
[95] E. Iancu and R. Venugopalan, in *Quark Gluon Plasma*, edited by R. C. Hwa *et al.* (World Scientific, Singapore, 2003), pp. 249–3363.
[96] J. Mandula and M. Ogilvie, Phys. Lett. B **185**, 127 (1987).
[97] G. D. Moore and N. Turok, Phys. Rev. D **56**, 6533 (1997).
[98] A. Krasnitz, Y. Nara, and R. Venugopalan, Phys. Rev. Lett. **87**, 192302 (2001).
[99] W. Florkowski, R. Ryblewski, and M. Strickland, Phys. Rev. D **86**, 085023 (2012).
[100] P. Romatschke and M. Strickland, Phys. Rev. D **69**, 065005 (2004).
[101] P. Romatschke and M. Strickland, Phys. Rev. D **71**, 125008 (2005).
[102] P. Romatschke, Phys. Rev. C **75**, 014901 (2007).
[103] M. Martinez and M. Strickland, Phys. Rev. Lett. **100**, 102301 (2008).
[104] A. Dumitru, Y. Guo, and M. Strickland, Phys. Lett. B **662**, 37 (2008).
[105] M. Martinez and M. Strickland, Phys. Rev. C **78**, 034917 (2008).
[106] A. Dumitru, Y. Guo, A. Mocsy, and M. Strickland, Phys. Rev. D **79**, 054019 (2009).
[107] A. Majumder, B. Muller, and S. Mrowczynski, Phys. Rev. D **80**, 125020 (2009).
[108] A. Dumitru, Y. Guo, and M. Strickland, Phys. Rev. D **79**, 114003 (2009).
[109] Y. Burnier, M. Laine, and M. Vepsalainen, Phys. Lett. B **678**, 86 (2009).
[110] O. Philipsen and M. Tassler, arXiv:0908.1746.
[111] M. Mannarelli, C. Manuel, S. Gonzalez-Solis, and M. Strickland, Phys. Rev. D **81**, 074036 (2010).
[112] M. Margotta, K. McCarty, C. McGahan, M. Strickland, and D. Yager-Elorriaga, Phys. Rev. D **83**, 105019 (2011).
[113] M. Strickland, Phys. Rev. Lett. **107**, 132301 (2011).
[114] M. Strickland and D. Bazow, Nucl. Phys. **A879**, 25 (2012).
[115] M. E. Carrington, K. Deja, and S. Mrowczynski, Acta Phys. Pol. B **5**, 947 (2012).
[116] P. M. Chesler and L. G. Yaffe, Phys. Rev. Lett. **102**, 211601 (2009).
[117] R. A. Janik and P. Witaszczyk, J. High Energy Phys. 09 (2008) 026.
[118] P. M. Chesler and L. G. Yaffe, Phys. Rev. D **82**, 026006 (2010).
[119] D. Mateos and D. Trancanelli, Phys. Rev. Lett. **107**, 101601 (2011).
[120] D. Mateos and D. Trancanelli, J. High Energy Phys. 07 (2011) 054.
[121] M. P. Heller, D. Mateos, W. van der Schee, and D. Trancanelli, Phys. Rev. Lett. **108**, 191601 (2012).
[122] P. M. Chesler and D. Teaney, arXiv:1112.6196.
[123] M. Chernicoff, D. Fernandez, D. Mateos, and D. Trancanelli, J. High Energy Phys. 08 (2012) 100.
[124] M. Chernicoff, D. Fernandez, D. Mateos, and D. Trancanelli, J. High Energy Phys. 08 (2012) 041.
[125] D. Giataganas, J. High Energy Phys. 07 (2012) 031.
[126] A. Rebhan and D. Steineder, J. High Energy Phys. 08 (2011) 153.
[127] A. Rebhan and D. Steineder, Phys. Rev. Lett. **108**, 021601 (2012).
[128] A. Rebhan and D. Steineder, J. High Energy Phys. 08 (2012) 020.
[129] J.-P. Blaizot, F. Gelis, J.-F. Liao, L. McLerran, and R. Venugopalan, Nucl. Phys. **A873**, 68 (2012).
[130] J. Berges and D. Sexty, Phys. Rev. Lett. **108**, 161601 (2012).
[131] J. Berges, S. Schlichting, and D. Sexty, Phys. Rev. D **86**, 074006 (2012).
[132] A. Kurkela and G. D. Moore, Phys. Rev. D **86**, 056008 (2012).
[133] S. Schlichting, Phys. Rev. D **86**, 065008 (2012).
[134] A. Krasnitz, Nucl. Phys. **B455**, 320 (1995).
[135] J. Ambjorn and A. Krasnitz, Phys. Lett. B **362**, 97 (1995).
[136] G. D. Moore, Nucl. Phys. **B480**, 689 (1996).
[137] D. Y. Grigoriev, V. Rubakov, and M. Shaposhnikov, Phys. Lett. B **216**, 172 (1989).
[138] J. Ambjorn, T. Askgaard, H. Porter, and M. Shaposhnikov, Nucl. Phys. **B353**, 346 (1991).